Geochemical Enhancement Of Enhanced Geothermal System Reservoirs: An Integrated Field And Geochemical Approach

Final Technical Report
September 30, 2007

DE-FG36-04GO14292

Principal Investigator: Joseph Moore; Energy and Geoscience Institute; 801-585-6931; jmoore@egi.utah.edu
Technical Contact Shirley Streff, 801-585-9763; Energy and Geoscience Institute; sstreff@egi.utah.edu

DOE Project Officer: Jay Nthwani; 303-275-4756; jay.nathwani@go.doe.gov
DOE Contract Spec: Pete Simon; 303-275-4787; pete.simon@go.doe.gov

Introduction

The geochemical effects of injecting fluids into geothermal reservoirs are poorly understood and may be significantly underestimated. Decreased performance of injection wells has been observed in several geothermal fields after only a few years of service, although the reason for these changes has only recently been established (McLin et al., 2006a). The goal of this project is to improve reservoir performance by understanding the effects of fluid injection on the reservoir and by providing solutions for mitigating these effects. The two geothermal fields that are the focus of this project are the Coso and Salton Sea geothermal fields, CA. Mineral deposition was hypothesized as the cause for declines in injection well performance.

These systems provide a unique opportunity to characterize injection-induced effects. During the initial phase of the project, rock samples from original and redrilled injection wells at Coso and Salton Sea were used to characterize the mineral and geochemical changes that occur as a result of injection. Samples from the original and redrilled injection wells at Coso were used to establish the mineral assemblages and their geochemical characteristics prior to injection. The results of these investigations were used to constrain numerical modeling of fluid-rock interactions and mineral changes in the near well bore environment. Future work includes predicting mineral deposition and dissolution in the reservoir rocks downstream of the injection wells.

Project Team

The members of the project team consist of Drs. J. Moore (Energy & Geoscience Institute and D. Norman (New Mexico Institute of Mining and Technology) who serve as Co-Principal Investigators, Dr. J. Park, a researcher at the New Mexico Institute of Mining and Technology and Ms. K. McLin, a Ph.D student at the University of Utah. CalEnergy Operating Corp., Calpine Corp. and Coso Operating Co. have generously provided

samples and data for the project. Dr. J. Bowman (University of Utah) is providing additional assistance in the interpretation of the geochemical data..

Work Plan

The proposed work plan for this project is shown in Figure 1. The project was funded through year 2 and was successful in meeting its objectives to that point. During the second year of the project, DOE requested that Dr. Moore provide additional support to the Coso EGS program and the objectives of the project were modified. At the time the project was terminated at the end of year 2, the objectives of the project were to:

1. Provide petrologic and geochemical support to the Coso EGS project
2. Conduct geologic investigations of Coso well 46A-19RD.
3. Determine the effects of fluid injection on Coso reservoir rocks through examination of drill hole samples.
4. Utilize these observations to constrain predictions of fluid-rock interactions.
5. Improve reservoir performance by developing injection strategies for mitigating and reversing the potential effects of mineral deposition resulting from injection.

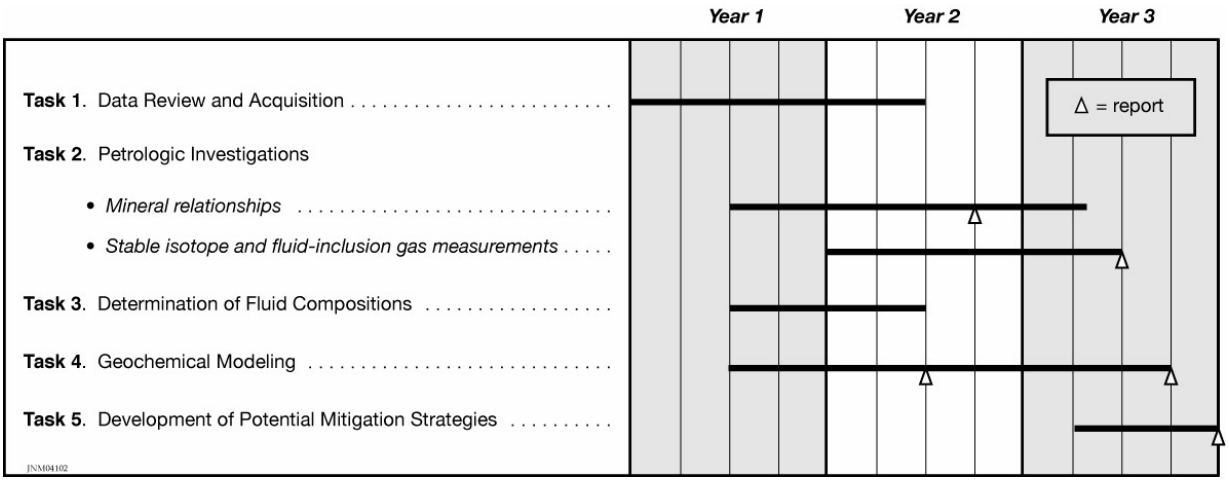

Fig. 1. Project work plan.

Approach

The basic approach of this study is to compare the mineral and geochemical signatures of the reservoir rock before and after injection. We will use samples from original injection wells to characterize rock conditions before injection began. At Coso, and the Salton Sea some of the original injection wells had to be redrilled because their performance had declined to the point where they could no longer accept the quantity of fluid that had to be injected. These declines occurred over a period of 5 to 7 years. Mineral deposition is the likely cause of their reduced performance. Samples from these redrilled injection wells, which were drilled adjacent to the original wells, will used to characterize the

effects of injection. Because the injected fluids are not in equilibrium with the reservoir rocks, mineral precipitation and dissolution can be expected to occur.

The Coso Geothermal System

The Coso geothermal field is developed in Mesozoic granitic rocks of the Sierra Nevada Batholith on the western edge of the Basin and Range (Adams et al, 2000). The heat driving the geothermal activity is related to shallow intrusions that have given rise to 38 rhyolitic domes during the last million years. The reservoir host rocks range in composition from diorite to granite with varying degrees of alteration and veining (Kovac et al, 2005). Active and fossil fumaroles lie along a NE-SW trending belt that extends through Devil's Kitchen and Coso Hot Springs. On the eastern margin of the field, known as the East Flank, fossil sinter and travertine deposits are present (Adams et al, 2000). Geothermal power production has been sustained at 240 MWe since 1989. Between 1987 and 1993, six injection wells were drilled on the 68-20 pad and four were drilled on the 67-17 pad in the southern part of the field (Fig. 2 and 3, Table 1). Reservoir temperatures prior to injection ranged from approximately 205-240^{o}C. The temperatures of the fluids injected into 68-20 ranged from 110-120^{o}C. The injected fluids had silica contents ranging from 174 to 965 ppm and were supersaturated in silica with respect to quartz, the stable silica phase in the reservoir (Table 2).

Occurrence of Scale Deposits Within the Reservoir Rocks

Cuttings from Coso injection wells have been examined at 3 m depth intervals. The rock type, the abundance of primary and secondary minerals, and the abundance, mineralogy, and paragenesis of the veins was documented at each interval. Thinly banded opaline silica was observed in the cuttings from 68-20RD and 68B-20RD, but not in the original drill holes or other wells. The banding and textural relationships suggest the silica represents fracture fillings and not alteration of preexisting minerals. The greatest density of silica precipitation was found in cuttings from depths of 2851-2900 ft. (869-884 m) and 5610-5620 ft. (1710-1713 m) (Fig. 4 and 5). Samples of the precipitate from these two zones were analyzed using a Scanning Electron Microscope (SEM) and X-ray diffractometer.

Table 1. Principal facts of Coso 68-20 and 67-17 pad injection wells.

WELL	TD Ft	TVD Ft	Completion Date	Scale Present
68-20	6485 (1977 m)	6473 (1973 m)	10/29/1987	No
68-20RD	7494 (2284 m)	7462 (2274 m)	5/8/1992	Yes
68A-20	7905 (249 m)	7608 (2319 m)	7/2/1988	No
68A-20RD	7011 (2137 m)	6918 (2109 m)	9/14/1988	No
68B-20	6782 (2067 m)	6771 (2064 m)	11/10/1988	No
68B-20RD	7058 (2151 m)	7019 (2139 m)	1/26/1993	Yes
67-17RD	9630 2935 m)	9335 (2845 m)	12/24/1991	No
67A-17	9427 (2873 m)	9199 (2804 m)	8/10/1992	No
67B-17	8900 (2713 m)	8619 (2627 m)	10/10/1994	No
67C-17	7813 (2381 m)	7646 (2331 m)	1997	No

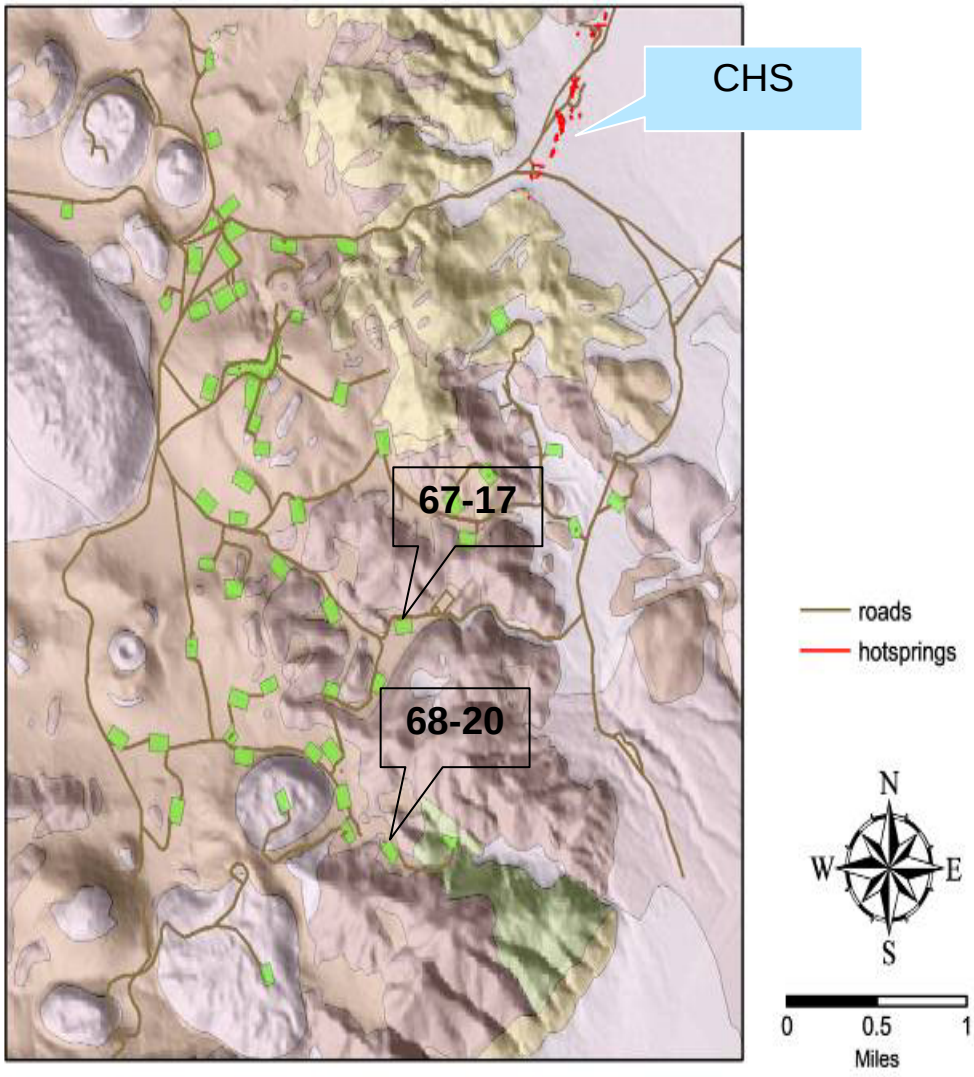

Fig. 2. Locations of the injection well sites. Green rectangles are well pads. CHS = Coso Hot Springs.

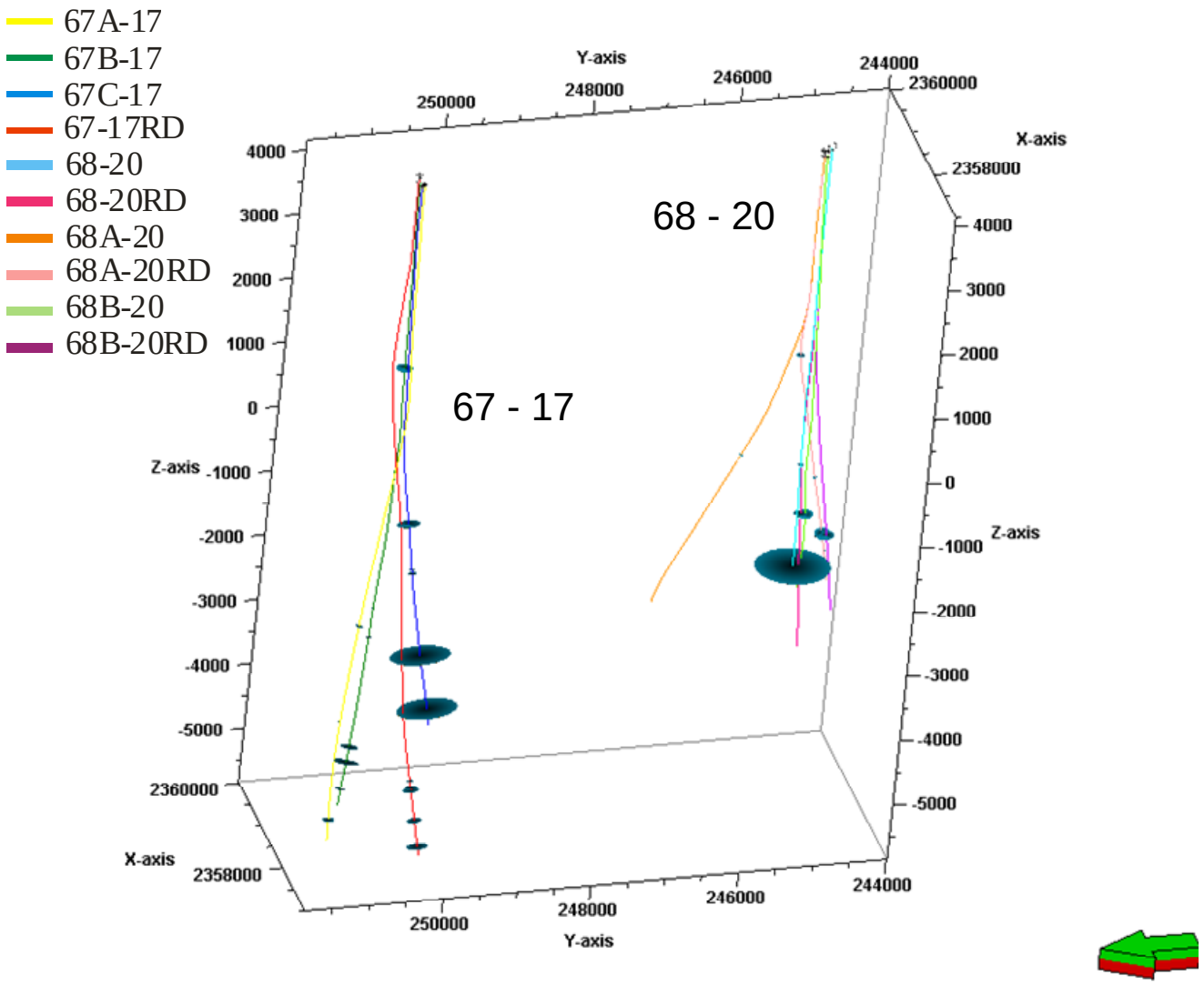

Fig. 3. Well trajectories and locations of lost circulation zones, shown as discs. The amount of fluid lost is represented by the size of the disc. Axes in feet.

Table2. Injected fluid chemistry from well 68-20 and 67C-17. Analyses are in mg/kg. The fluids were injected at 110- 120°C (220-240°F).

Well	Date	Na	K	Ca	Mg	Fe	Al	SiO_2	B	Li	Sr
68-20	6/27/1988	3340	725	78.1	8.7	33.2	10.4	555	99.7	37.2	3.3
68-20	10/4/1988	3520	941	64.4	0.27	0.49	0	965	116	47	3.8
68-20	3/30/1989	2897.17	362.27	19	0.08	0.3	0.37	617.14	87.99	24.57	2.79
68-20	6/15/1989	2993.2	464.5	22	0.09	0.13	0.56	677.76	83.02	40.74	2.6
68-20	9/27/1989	3652	501	29	0.14	0.01	0.25	173.51	119.21	33.14	3.67
68-20	11/13/1989	3470	579.57	25	0.12	2.53	0.63	697.51	114.14	31.39	3.9
68-20	1/7/1990	3540	590.16	24	0.15	1.88	0.39	826.4	128.95	35	3.62
68-20	4/20/1990	4283	633.44	36	0.65	84.1	1.58	747.15	126.64	35	6.01
68-20	8/19/1990	4010	739	32	0.14	2.85	0.5	936.23	141.8	40	3.66
68-20	10/12/1990	3908	672	38	0.15	0.33	0.33	701.49	121	36.7	4.88
68-20	2/3/1991	3774	595	47.3	0.46	0.12	0	545	109	31.3	4.42
68-20	5/7/1991	3480.37	605.28	37.16	0	0.88	0	592.51	112.68	28.16	4.95
68-20	8/3/1991	4192	590	130	3.94	6.5	1.01	620.4	130	30	8.23
68-20	11/21/1991	3508.3	601.35	46.4	0.14	0.3	0.43	545.92	125.16	30.78	5.51
68-20	12/13/1996	876	147	18	ND	1.7	ND	97	36	6.8	1.8
67C-17	1/23/98	1670	350	39	ND	ND	ND	373	74	14	1670

ND = not determined.

Well	Date	As	Ba	HCO_3	Cl	F	SO_4	TDS	Lab pH
68-20	6/27/1988	9.2	0.8	229	5770	2.4	73	10900	6.77
68-20	10/4/1988	11.2	116	77	6600	2.8	27	12300	7.2
68-20	3/30/1989	8.33	0.47	156	5015	2.33	80	9233	6.82
68-20	6/15/1989	10.94	0.4	195	5465	2.2	90		7.25
68-20	9/27/1989	10.15	0.69	178	6440	1.7	95	11237	7.45
68-20	11/13/1989	6.9	0.56	168	5165	1.64	71		6.83
68-20	1/7/1990	8.02	0.58	224.5	6018	2.3	44		6.73
68-20	4/20/1990	26.24	0.9	141.5	5698	5.7	90		6.723
68-20	8/19/1990	7.22	0.58	151	6958	3.01	27		7.3
68-20	10/12/1990	8.8	0.9	161	6618	2.12	47		8.2
68-20	2/3/1991	6.68	2.44	161	6340	2.48	99	11550	8.2
68-20	5/7/1991	2.85	0	174	6070	2.2	87	11000	8.3
68-20	8/3/1991	10.9	1.64	185.44	6855	2.8	53		8.16
68-20	11/21/1991	6.1	0.8	143	6100	1.94	72	11500	8.25
68-20	12/13/1996	1.9	0.3	7.5	1412	ND	59	2766	6.17
67C-17	1/23/98			ND	3270	ND	38	6390	ND

ND = not determined

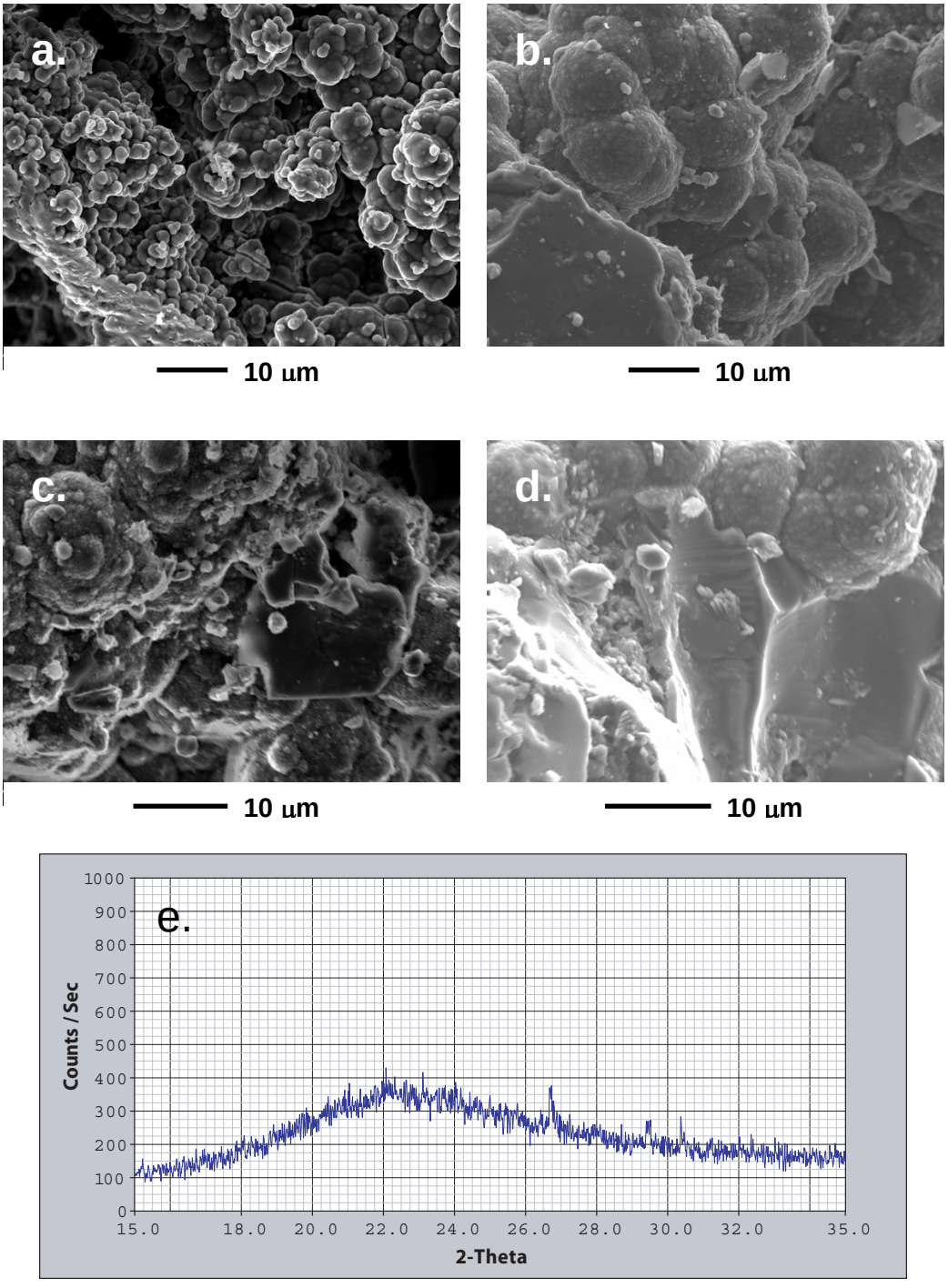

Fig. 4 (a).-(d). SEM images from 68-20RD at 2851-2900 ft. (869-884 m) depth. Opal-A spheres 1-2 mm in diameter seen in (a). coalesce to form 10 mm spheres and sheets (b, c and d).. (e). X-ray diffraction pattern of the scale showing a broad opal-A peak centered at 22^{o} 2-theta and quartz peaks at 21.5^{o} and 26.8^{o} 2-theta.

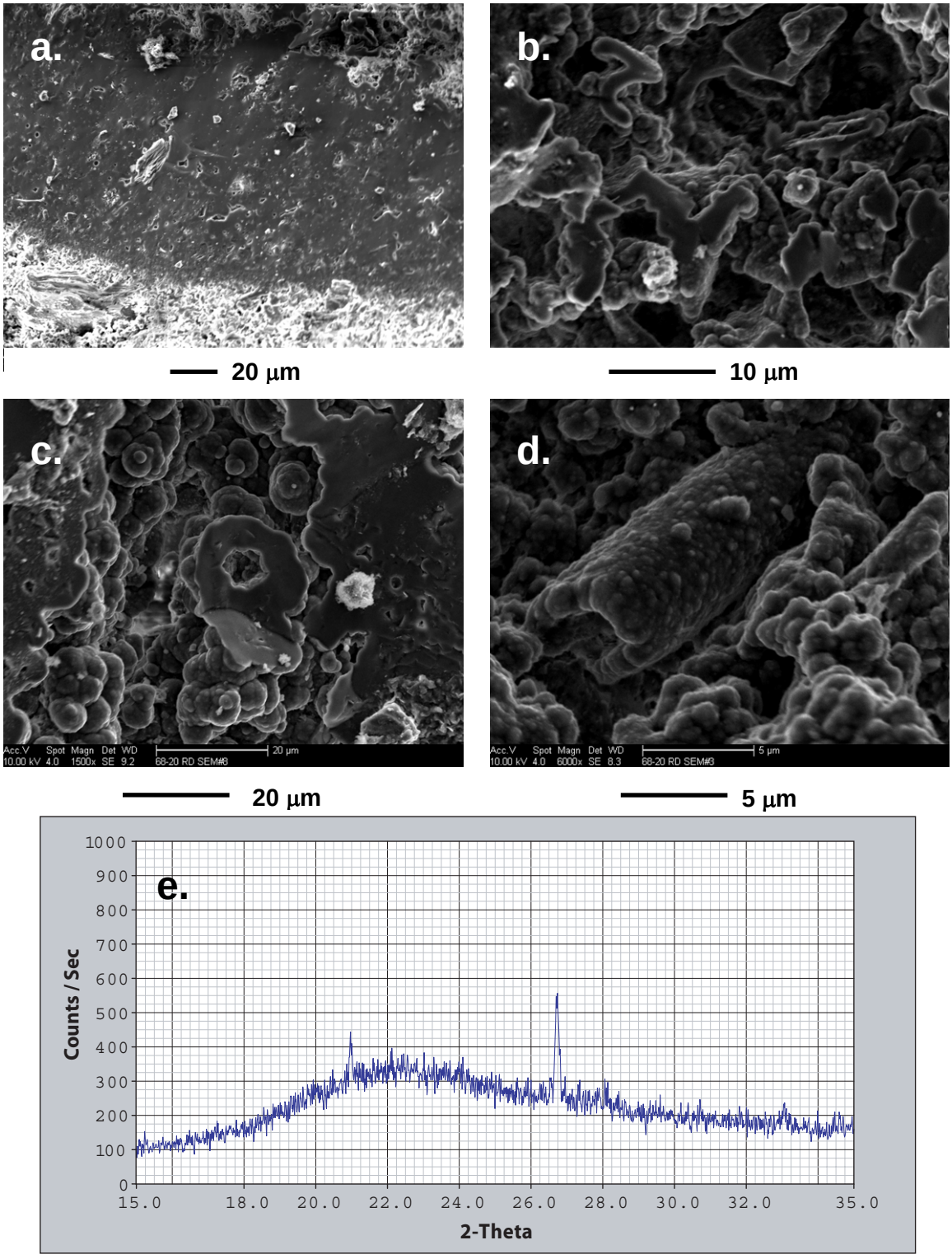

Fig. 5. (a).-(d). SEM images from 68-20RD at 5610-5620 ft. (1710-1713 m) depth. (a). Alternating silica layers with varying density and visible porosity. (b), (c). Silica spheres aligning to form strands (b). and sheets (c). (d). Tube structure covered with silica spheres. (e). X-ray diffraction pattern of the scale showing a broad opal-A peak centered at 22^{o} 2-theta and quartz peaks at 21.5^{o} and 26.8^{o} 2-theta.

The silica deposits consist of opal-A spheres and plates. Figures 4 and 5 show the morphological progression associated with maturation of the deposits. Textural relationships shown in Figure 4A indicate the silica was deposited initially as spheres 1-2 μm in diameter. As the deposits mature, the spheres coalesce to form larger spheres up to 10 μm in diameter (Fig. 4b). Further maturation is associated with the formation of plates and sheets (5b, c). Infilling of the spaces between spheres provides a possible explanation for the dense, smooth surfaces seen in Figures 4a. Traces of calcite locally coat the amorphous silica, suggesting it represents a later stage in the evolution of the deposits. The SiO_2 maturation sequence observed at Coso is closely follows the changes observed in sinter deposits (Rodgers et al, 2004; Lynne and Campbell (2004).

An interesting and unusual feature of the silica deposit from 5610-5620 ft (1710-1713 m). s the tube like structure coated with silica spheres (Fig. 5d). Similar features, interpreted as silicified bacteria, have been observed in sinters from New Zealand (Rodgers et al, 2004).

The X-ray diffraction patterns of the samples are characterized by a broad peak centered at 22^o 2-theta representing opal A, and peaks at 21.5^o and 26.8o 2-theta representing quartz. Although quartz was not documented in the SEM images, it is possible that it represents fragments of the host reservoir rock. Alternatively, it is possible, but less likely, that the quartz represents maturation of the opal-A. Although quartz is common in mature sinter deposits, there is no evidence from the SEM or X-ray diffraction studies of intermediate stage in the Coso rocks.

Fluid Inclusion Gas Analyses

The gas contents and distribution of gaseous species in fluid inclusions were measured to determine if changes in the compositions of the inclusions could be used as a subtle indicator of interactions between the reservoir rocks and the injected injected fluids. It was hypothesized that the intrusive reservoir rocks would be characterized by fluid inclusions with high gas/water ratios. In contrast, the injected fluid has a low gas/water ratio because the fluid is flashed and the gases are transferred to the steam phase before the liquid is reinjected. Condensate that equilibrates with the atmosphere in the cooling tower will also have a relatively low gas/water ratio.

We are able to test this hypothesis by analysis of chips from 68-20, collected before injection began, and from 68-20 RD, drilled to replace the original well 5 years later (Dilley et al., 2006; Norman et al., 2007). Figure 6 compares the H_2O and total gas distributions in 68-20 and 68-20 RD; ratios of CO_2/H_2O are shown in Figure 7. Fluid Inclusion Technologies performed the analyses on drill cuttings collected at 6 m intervals. Chips are crushed in vacuum and the volatiles released are analyzed by quadrupole mass spectrometry.

The analyses show that fluid inclusion gas/water ratios decreased by about 60% whereas the amount of inclusion water was about the same for both suites of chips. These changes are most pronounced in areas of high fluid flux where silica scale was deposited at depths

of 2851-2900 (869-884 m) and 5610-5620 ft, (1710-1713 m) but the changes extend well beyond portions of the reservoir rock that contain the scale.

Differences between the two sets of analyses require the opening and loss of gaseous species from over 50% of the wall rock fluid inclusions. Furthermore the data show that the destruction of the original inclusions and formation of new fluid inclusions can occur rapidly, within a few years. Thus it is possible to use the bulk fluid inclusion gas analyses of drill cuttings to track the migration of the injected water. An important implication of this work is that the bulk-geochemical analyses will be biased towards the most recent event. Thus, the plots show that differences in the gas/water ratios provide a subtle record of interactions between the reservoir rocks and injected fluids, and that these changes can be used to track the movement of the injected fluids beyond areas where scale deposition has occurred.

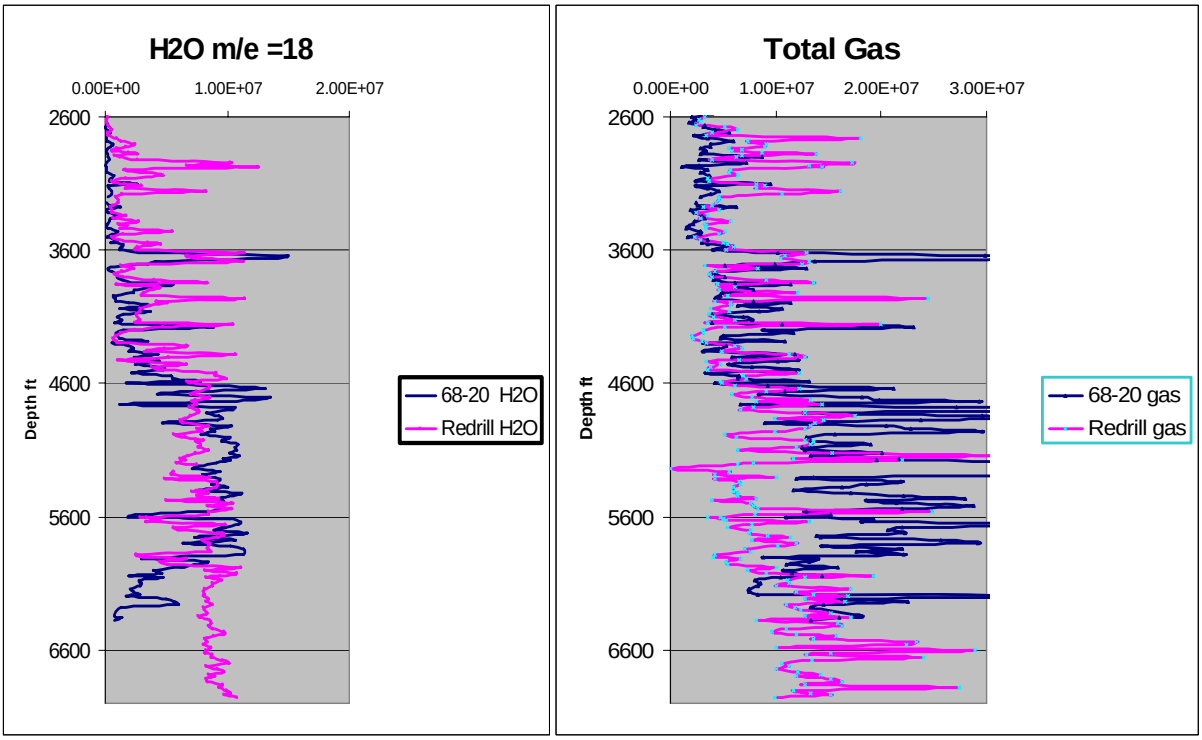

Fig. 6. Distribution of H_2O and total gas in 68-20 and 68-20 RD.

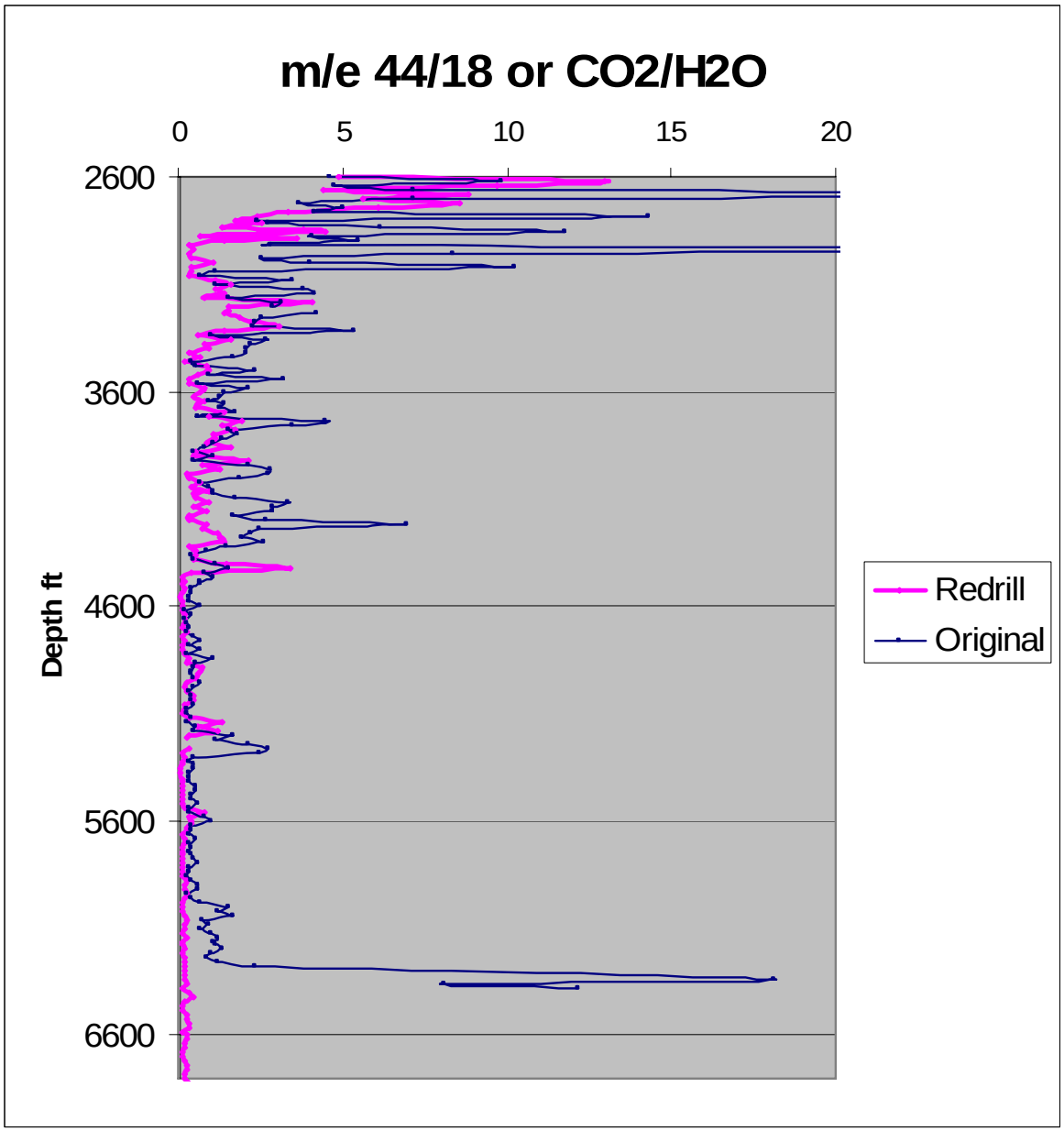

Fig. 7. Distribution of CO_2/H_2O ratios in 68-20 and 68-20 RD.

Geochemical Modeling of Fluid Rock Interactions

Geochemical simulations were carried out by McLin et al. (2006b)using the non-isothermal reactive geochemical transport code TOUGHREACT (Xu and Pruess, 2001; Xu et al., 2004). This code was developed by introducing reactive chemistry into the framework of the existing multi-phase fluid and heat flow code TOUGH2 V2 (Pruess et al., 1999, see also http://www-esd.lbl.gov/TOUGHREACT/). Interactions between mineral assemblages and fluids can be modeled assuming local equilibrium or using kinetic rates. The gas phase can be chemically active. Precipitation and dissolution reactions can change formation porosity and permeability, as well as modify the unsaturated flow properties of the rock. This simulator can be applied to 1-, 2-, and 3-dimensional porous and fractured media with physical and chemical heterogeneity. It can also deal with any number of species present in the liquid, solid, and gaseous phases.

The geometry and fluid and heat flow conditions are modeled after those described in Xu and Pruess (2004). A one-dimensional MINC (multiple interacting continua) model was used to represent the fractured rock. The MINC method can resolve "global" flow and diffusion of chemicals in the fractured rock and its interaction with "local" exchange between fractures and matrix. Details on the MINC method for reactive geochemical transport are described by Xu and Pruess (2001). In the simulations we considered interactions with: 1) a zone representing the relatively impermeable, unaltered host rock; and 2) altered, fractured, and veined host rock. In addition we considered two different rock types, diorite and granodiorite, which are the dominant lithologies affected by the injected fluid and where silica deposition has occurred. The parameters used in the models are shown in Table 3. A density of 2650 $kg*m^{-3}$, heat capacity of 1000 $J*kg^{-1}K^{-1}$, and diffusivity of 10^{-9} $m^{-2}s^{-1}$ were used for all zones. The cubic law was used to define the porosity-permeability relationship in both zones (Xu et al., 2004). The model generates changes in porosity and permeability based on changes in mineral abundances.

Table 3. Parameters used in the numerical simulations.

Parameters	Fracture	Average Weakly-Altered Granodiorite	Average Weakly-Altered Diorite
Volume (m^3)	0.1	0.9	0.9
Permeability (m^2)	2.0E-12	2.0E-18	2.0E-15
Porosity	0.10	0.02	.05
Thermal Conductivity ($W* m^{-1}K^{-1}$)	2.9	3.0	3.0
Tortuosity	0.3	0.1	0.1

The reservoir rocks at a depth of 878 m in 68-20RD are dominated by hornblende biotite quartz diorite. Biotite granodiorite dominates at 1710 m. The mineralogical

compositions of these rocks were estimated from thin section observations of samples from 68-20RD and from X-ray diffraction and thin section studies of East Flank wells by Kovac et al (2005) and Lutz and Moore (1997). Both rock types are only weakly altered in 68-20RD. Veining is especially weak in the diorite at 878 m; consequently the fracture zone was modeled as nearly empty. The deeper granodiorite was contains quartz, calcite and chlorite veins, as shown in Table 4.

Table 4. Mineralogy of the reservoir rocks.

Mineral	Volume Fraction of Solid Rock			
	1710 m: Granodiorite-hosted		878 m: Diorite-hosted	
	Average Weakly-Altered Granodiorite	Fracture	Average Weakly-Altered Diorite	Fracture
Quartz	0.34	.05	.135	
Potassium Feldspar	0.17		.045	
Chlorite	0.02	.01	.01	
Illite	0.03		0.00	
Calcite	0.02	.04	.025	.009
Anorthite	0.33		.038	
Annite	0.06		0.15	

Mineral dissolution and precipitation are considered under kinetic constraints. The general kinetic rate expression used in TOUGHREACT (Xu et al., 2004) is given as follows:

$$r_m = \pm k_m A_m a_{H+}{}^n |1- Q_m/K_m| \qquad (1)$$

where m is the mineral index, r_m is the dissolution/precipitation rate, (positive for dissolution, negative for precipitation), k_m is the rate constant (moles per unit mineral surface area and unit time) which is temperature-dependent, A_m is the specific reactive surface area per kg of H_2O, a_{H+} is the activity of H^+, and n is an empirical reaction order accounting for catalysis by H^+ in solution. K_m is the equilibrium constant for the mineral-water reaction written for the destruction of one mole of mineral m, Q_m is the ion activity product. The temperature dependence of the reaction rate constant can be expressed as:

$$k = k_{25} \exp[-E_a/R(1/T-1/298.15)] \qquad (2)$$

where E_a is the activation energy, k_{25} is the rate constant at 25°C, R is the universal gas constant, and T is absolute temperature. Table 5 shows the parameters used in the kinetic rate expression.

Table 5. Parameters used in the kinetic rate expression

Mineral	k_{25} (moles m^{-2} s^{-1})	E_a (KJ/mole)	n (rxn. order)	Surface Area (cm^2/g)
Quartz	1.2589E-14	87.5	0	9.8
Am. Silica	7.3200E-13	60.9	0	1.0E6
	1.0000E-10	0.00	0	1.0E6
K-feldspar	1.0000E-12	57.78	0	9.8
Anorthite	1.0000E-12	57.78	0	9.8
Na-smectite	1.0000E-14	58.62	0	151.63
Ca-smectite	1.0000E-14	58.62	0	151.63
Illite	1.0000E-14	58.62	0	151.63
Annite	2.5119E-15	66.20	1	9.8
	2.5119E-15	66.20	0	9.8
Calcite	6.9183E-2	18.98	1	9.8
	6.4565E-7	62.76	0	9.8
Dolomite	1.0233E-3	20.90	1	9.8
	4.4668E-10	62.76	0	9.8
Chlorite	2.5119E-12	62.76	0	151.63

The composition of the reservoir fluid was estimated from the composition of an East Flank well (Table 6). Initial fluid compositions within the fracture and host rock were calculated by equilibrating the reservoir fluid composition with each rock's mineralogical composition at 275°C. An example injection fluid composition that is relatively enriched in Na^+, Cl^-, and $SiO_{2(aq)}$ was chosen as the trial injection water (Table 6). The injectate composition was not allowed to change over time.

Table 6. Compositions of reservoir and injected water used in the simulations.

Chemical Component	Reservoir (Mol/kg)	Injection (Mol/kg)
SiO_2	1.30E-2	9.96E-03
$B(OH)_3$	8.42E-3	1.01E-02
Na^+	9.50E-2	1.46E-01
K^+	1.20E-2	1.42E-02
Li^+	2.45E-3	4.44E-03
Ca^{2+}	9.55E-4	1.07E-03
Mg^{2+}	4.12E-6	2.22E-2
Sr^{2+}	3.60E-5	5.00E-2
Cl^-	1.10E-1	1.60E-01
F^-	1.47E-4	1.15E-04
HCO_3^-	1.10E-3	2.48E-03
SO_4^-	3.12E-4	6.97E-04
HS^-	3.02E-5	
CH_4	6.25E-10	
pH	6.84	6.47
As		1.16E-04

For the initial modeling, a one-dimensional multiple interacting continua (MINC) model was used. This conceptual model considers a one dimensional flow tube between the injection and production wells, which is a small sub-volume of the more extensive three-dimensional reservoir. The initial reservoir conditions were 275^{o}C and 30 MPa pressure. An over-pressure of 2 MPa was applied to the injection site. The model is based on conditions during nearly continuous injection over seven years. The control case model uses measured, observed, and estimated parameters from Lutz and Moore (1997), Kovac et al (2005), and McLin et al (2006). The simulations were run to a total time of 7 years. Changes in fluid pH, fracture porosity, fracture permeability, fluid temperature, and mineral abundances were monitored out to a distance of 594 m from the injection well. Mineral abundance changes, as changes in volume fraction for quartz, potassium feldspar, chlorite, illite, Na-smectite, Ca-smectite, calcite, dolomite, anorthite, biotite, and amorphous silica were determined. Amorphous silica, calcite, and quartz displayed the most significant changes. Changes in porosity were calculated as a function of mineral dissolution and precipitation. A porosity increase indicates that mineral dissolution is dominant, while a porosity decrease occurs when precipitation dominates. Changes in permeability were calculated from changes in porosity as described above.

In the modeled control case at both depths, amorphous silica precipitates soon after injection begins, followed by calcite and a very minor amount of quartz (Fig. 8), consistent with observed mineral deposits in the rocks. Amorphous silica deposition did not occur in the case where silica concentration was decreased in the injected fluid by an order of magnitude (Fig. 8c, 8e).

The majority of amorphous silica precipitated within a few meters of the well and a period of one year (Fig. 9). Mineral deposition is accompanied by significant porosity and permeability decreases within a few meters of the well over the same time period. Calcite also precipitates near the injection well. These results are consistent with the rapid (within a few months) decline in injectivity experienced by well 68-20 (Fig. 10). As predicted, amorphous silica was observed only within a few meters of the original well. Thus the modeled results closely simulate the observed mineral paragenesis and abundances based on analyses of the cuttings.

The effects of modifying the pH of the injection fluid, from acidic to basic, to mitigate the effects of silica deposition were investigated by Park et al. (2006). Acid injection reduces the kinetic rate of silica precipitation by reducing the pH. Although this inhibits SiO_2 deposition in the immediate vicinity of the injection well, deposition of SiO_2 can still be expected at greater distances. Injection of a basic solution will lead to SiO_2 undersaturation and dissolution by the formation of $NaHSiO_3$. Thus alternating the pH of the injected fluid may lead to enchanced permeabilities over time.

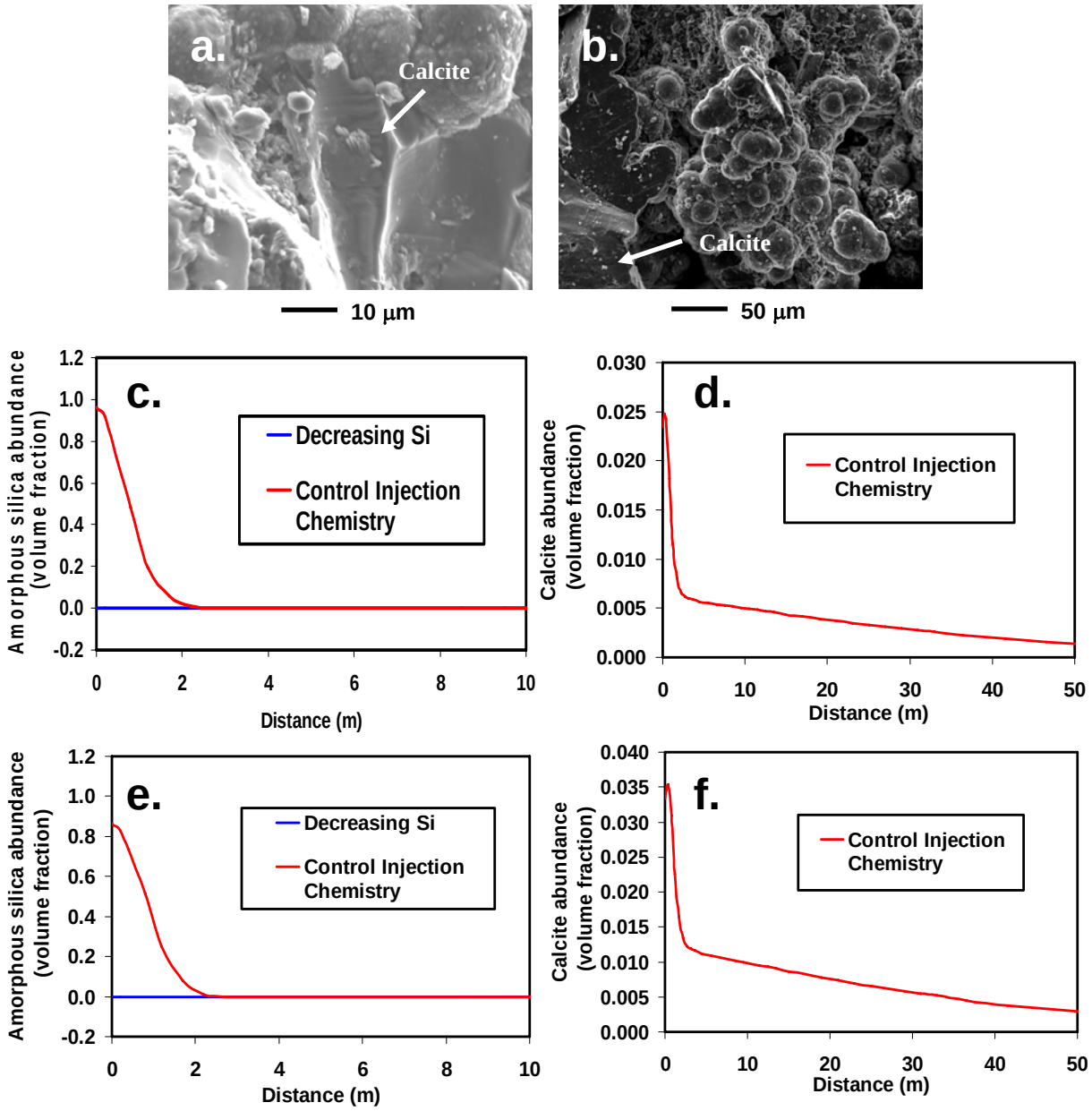

Fig. 8. (a). SEM image of opal-A and calcite from the depth interval 869-884 m. (b). SEM image of opal-A with small white calcite crystals from the depth interval 1710-1713 m. (c). and (d). Modeled results for a depth of 878 m showing amorphous silica (c) and calcite (d) as a function of distance in meters. (e) and (f) Modeled results for a depth of 1710 m showing amorphous silica (e) and calcite (f) as a function of distance in meters.

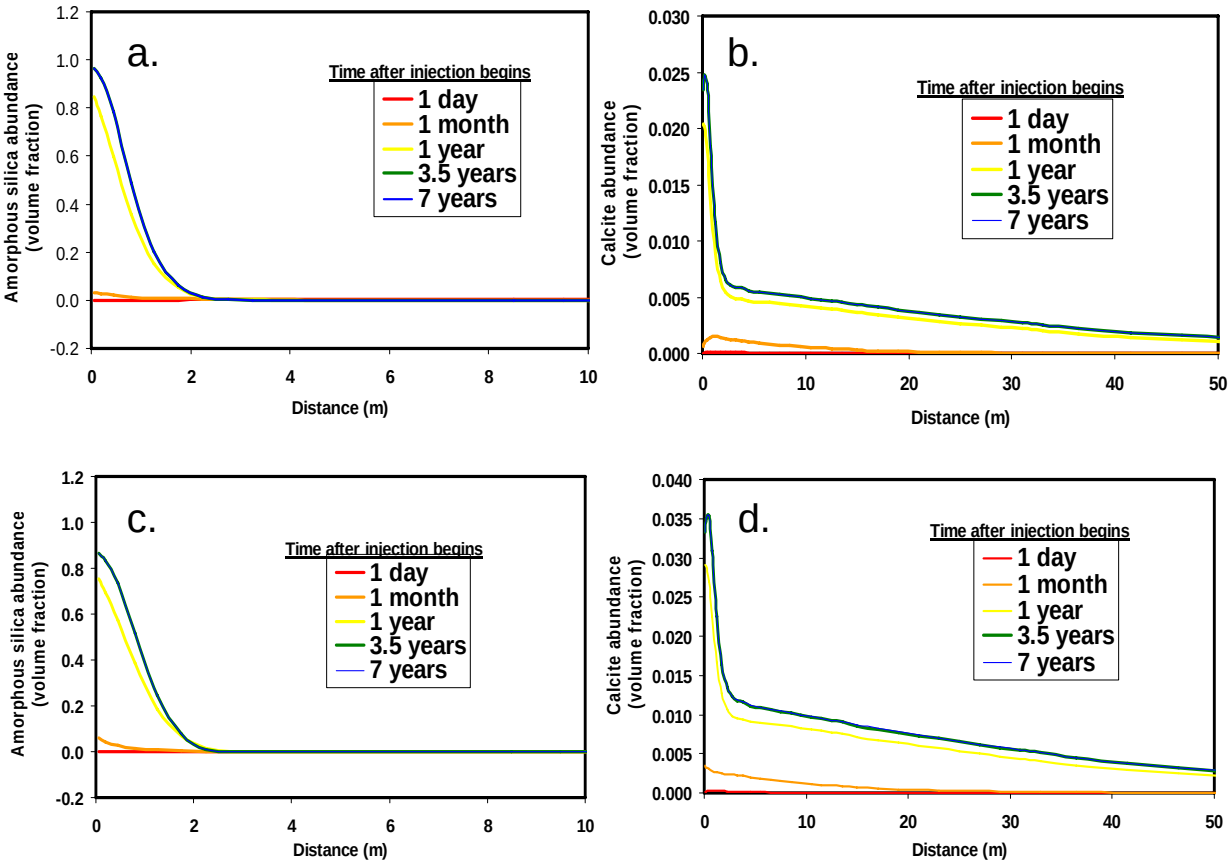

Fig. 9. Modeled results (a). and (b) from 878 m and (c), (d) from 1710 m showing amorphous silica and calcite as a function of distance in meters for various time periods over seven years.

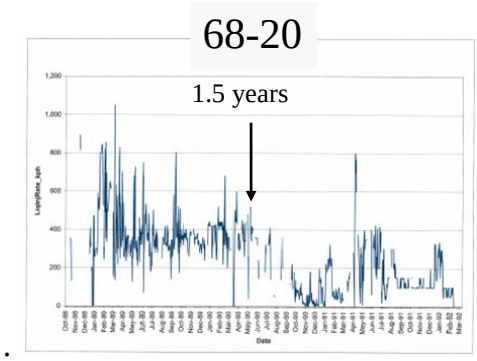

Fig. 10. Injection history of the original injection well 68-20.

Petrologic Investigations of Well 46A-19RD

Detailed petrographic studies of well 46A-19RD have been conducted to determine the regions that are most likely to fail during stimulation (Kovac et al., 2006). Rock type, the location and paragenesis of the hydrothermal mineral assemblages, intensity of hydrothermal alteration and the locations of past fracture zones and their relationships to zones of fluid flow have been defined. Well 46A-19RD is among the hottest of the wells drilled at Coso, reaching temperatures in excess of 300^{o}C (Fig. 11).

The rock types found in this well include quartz diorite, granodiorite, granite, and granophyre. In general, the lithologies encountered in this well are similar to those of other Coso wells with the exception of the granophyre, which has not been identified in any of the other wells studied so far.

Figure 11 shows that quartz diorite is the most common rock in the upper 11,500 ft (3505 m)and that at greater depths, granodiorite is the dominant rock type. Generally, the granodiorite in this well is more altered and veined than in the East Flank wells. The deep portion of the well also contained several zones of strong pervasive alteration, labeled ‘alteration zones’ by the mudloggers.

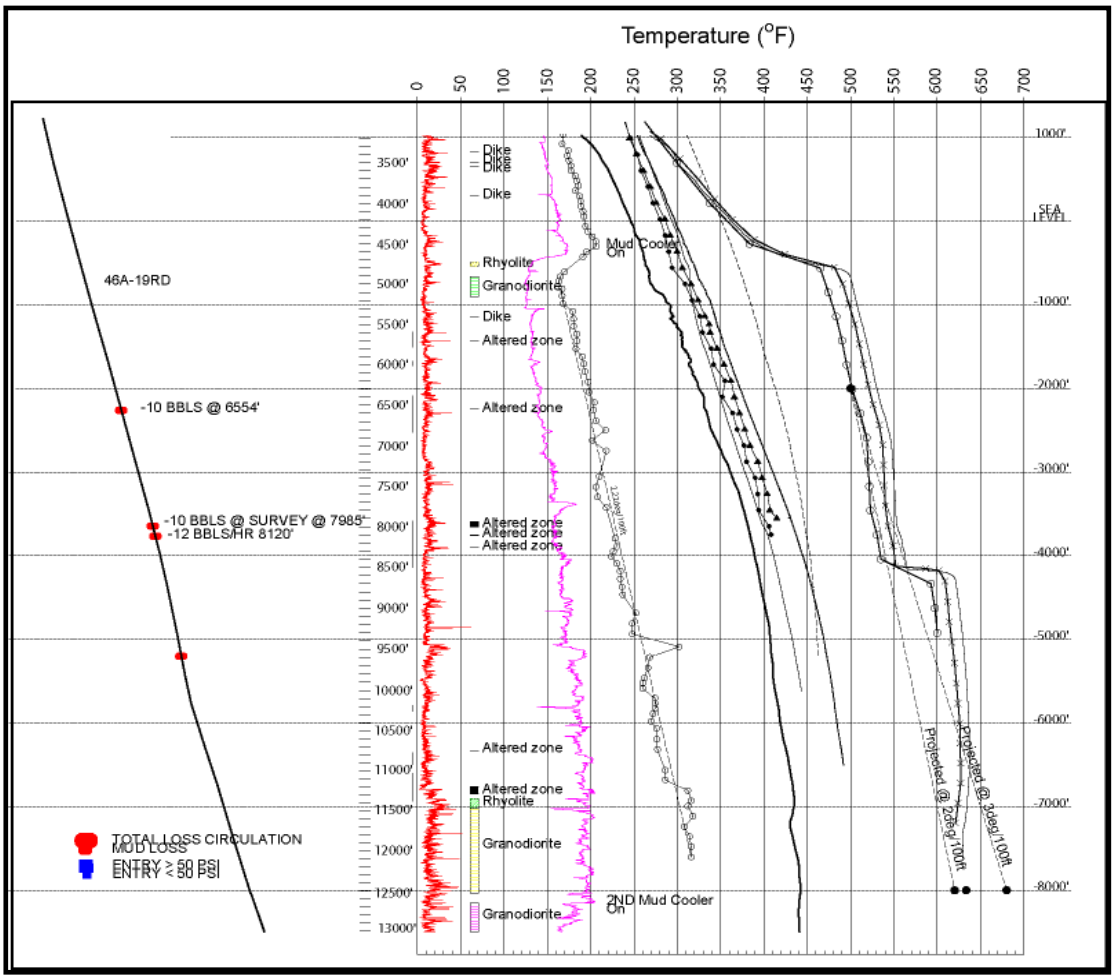

Fig. 11. The summary log for well 46A-19RD. Note the lack of lost circulation zones in the deep portion of the well. Also note the altered zones. See text for discussion.

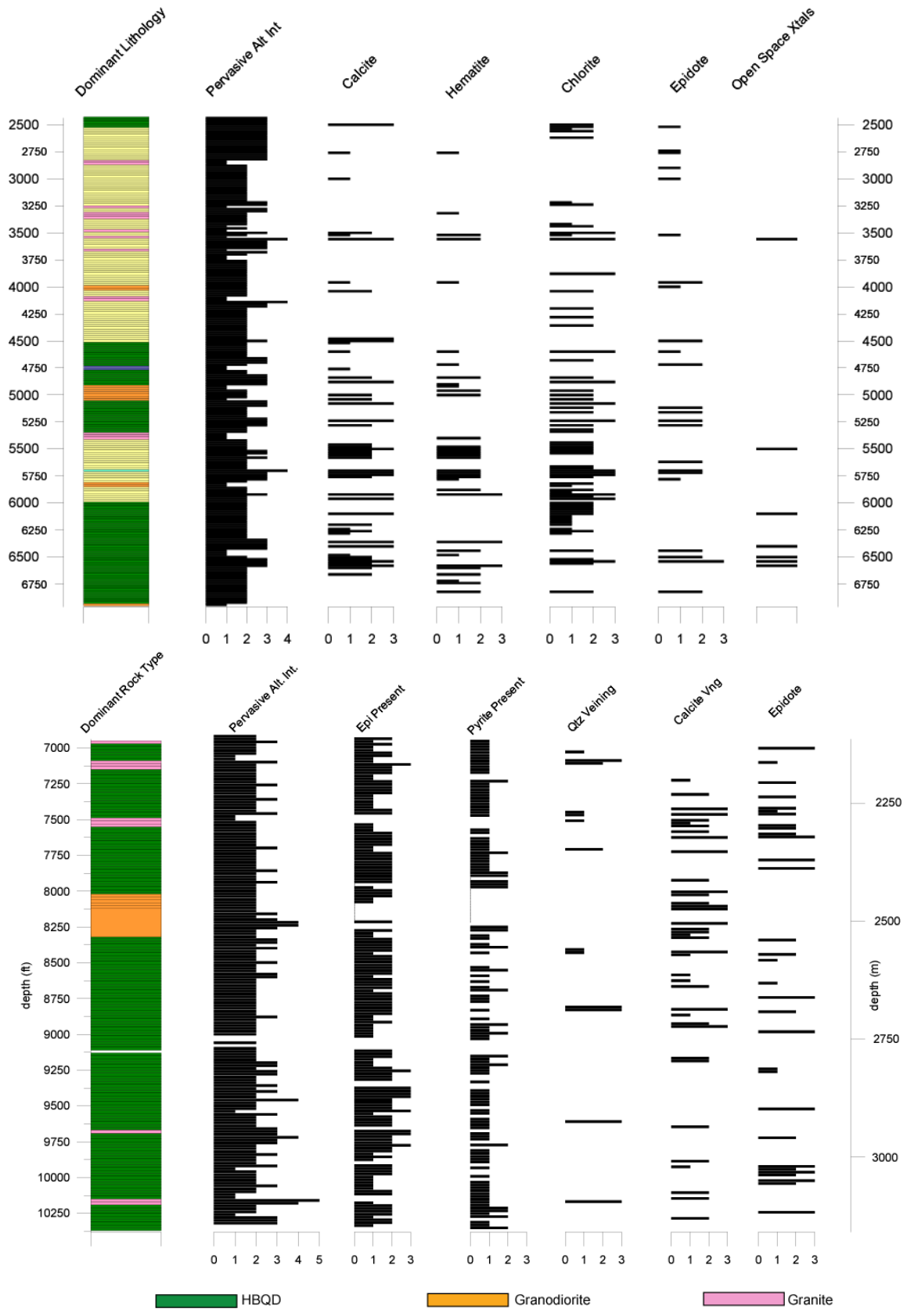
Dominant Lithology
Pervasive Alt Int
Calcite
Hematite
Chlorite
Epidote
Open Space Xtals
2500
2750
3000
3250
3500
3750
4000
4250
4500
4750
5000
5250
5500
5750
6000
6250
6500
6750
0 1 2 3 4
0 1 2 3
Dominant Rock Type
Pervasive Alt. Int.
Epi Present
Pyrite Present
Qtz Veining
Calcite Vng
Epidote
depth (ft)
7000
7250
7500
7750
8000
8250
8500
8750
9000
9250
9500
9750
10000
10250
0 1 2 3 4 5
depth (m)
2250
2500
2750
3000
HBQD
Granodiorite
Granite

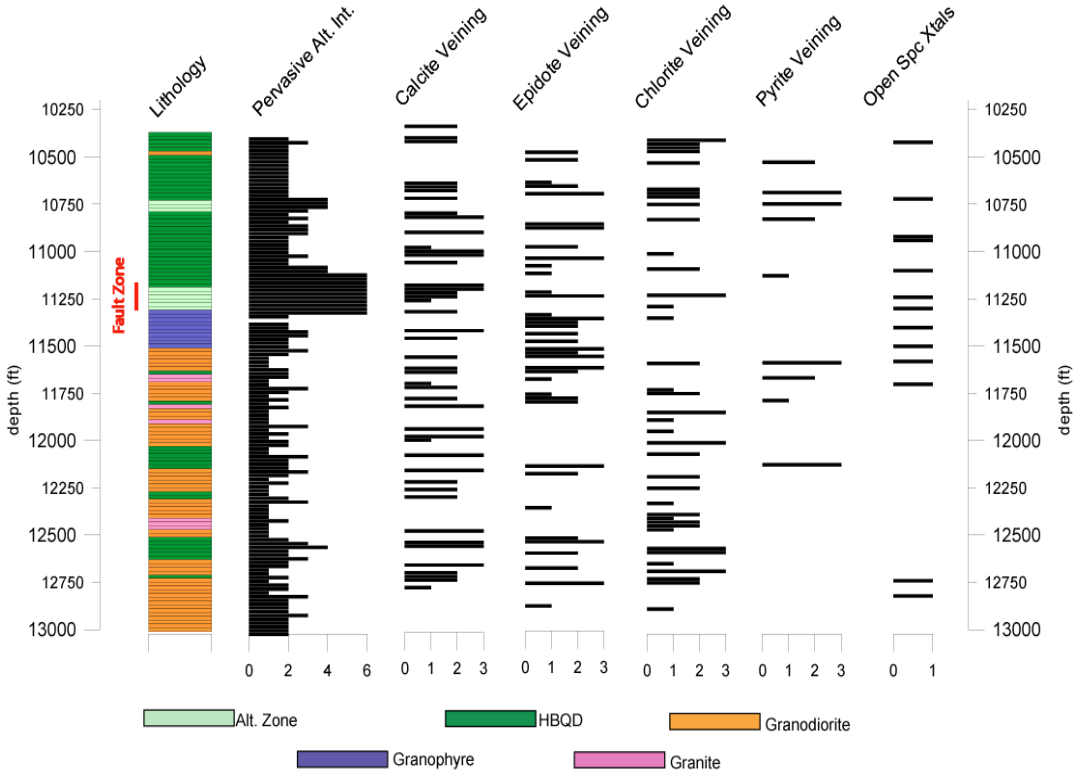

Fig. 11. Distributions of rock types, alteration intensity and hydrothermal minerals between depths of 2500 and 13,000 ft (762-3962 m) in well 46A-19RD. Lithology color code as follows: dark green = hornblende biotite quartz diorite, yellow = biotite quartz diorite, orange = biotite granodiorite, pink = granite, purple = granophyre, light green = alteration zone.

Hydrothermal Alteration Zones and Vein Mineralization

The altered zones can be readily identified in the chip samples by their green color and abundance of epidote, pyrite, chlorite, and white micas. This type of alteration occurs most commonly within narrow intervals of the hornblende biotite quartz diorite. Altered zones at about 6540 - 6560 ft (1993-1999 m) and 7940 - 8020 ft (2420-2445 m), correlate with zones of lost circulation.

The earliest vein assemblage consists of chlorite, epidote, pyrite, quartz, and minor sulfides (Fig. 12). This assemblage is characteristic of the oldest lithologies. The youngest assemblages are dominated by calcite $\pm$ chlorite, quartz, hematite, and minor wairakite. Minerals typical of both the cap rock (smectite, illite-smectite) and reservoir (epidote, wairakite, illite) sections of other wells have been identified in 46A-19RD. Two generations of epidote appear to be present, a coarse-grained epidote that forms sealed veins within the quartz diorite and granodiorite, and vuggy veins containing small euhedral crystals of green epidote. These small euhedral crystals may represent a younger generation of mineralization, perhaps geothermal in age. Similar epidote has been encountered in nearby well 72-19. In this well wairakite, which is characteristic of

geothermal systems, postdates the epidote at 6100 ft (1859 m). In general, temperatures implied by the minerals trend from hotter to cooler as time progresses. However, preliminary fluid inclusion studies on the youngest blocky calcite indicate temperatures consistent with the hot, present-day conditions.

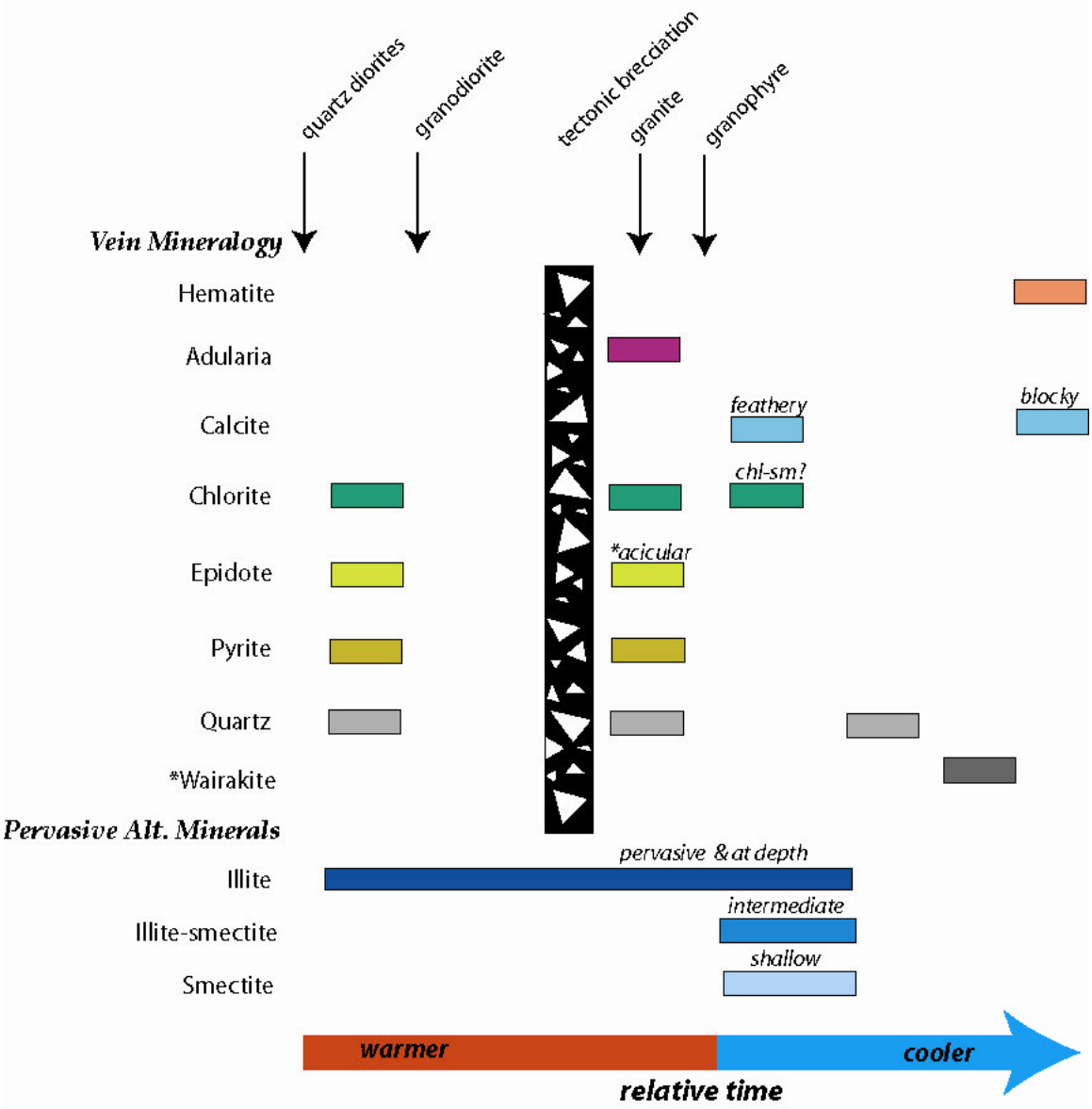

Fig. 12. The mineral paragenetic sequence based on observations from well 46A-19RD. Generally, the assemblages show a progression from hotter to cooler assemblages over time. See text for discussion.

Clay Mineralogy

X-ray diffraction analyses of select samples over the depth of the well were conducted. The clay minerals smectite, kaolinite, interlayered illite-smectite, illite, chlorite, and chlorite-smectite were identified. A summary of the clay mineralogy vs. depth is shown in Figure 13. The present day temperature profile is shown at the left. In geothermal systems, smectite is considered stable up to temperatures of 180°C (Henley and Ellis, 1983), and interlayered illite-smectite to temperatures of 225°C (Henley and Ellis, 1983.) In comparison to the present temperature profile, smectite's disappearance is consistent with the ~180°C depth. However, illite-smectite persists to depths where temperatures are much higher than 225°C. The persistence of these clays may be due to recent heating, or possibly low permeabilities, which has hindered reequilibration of the rocks.

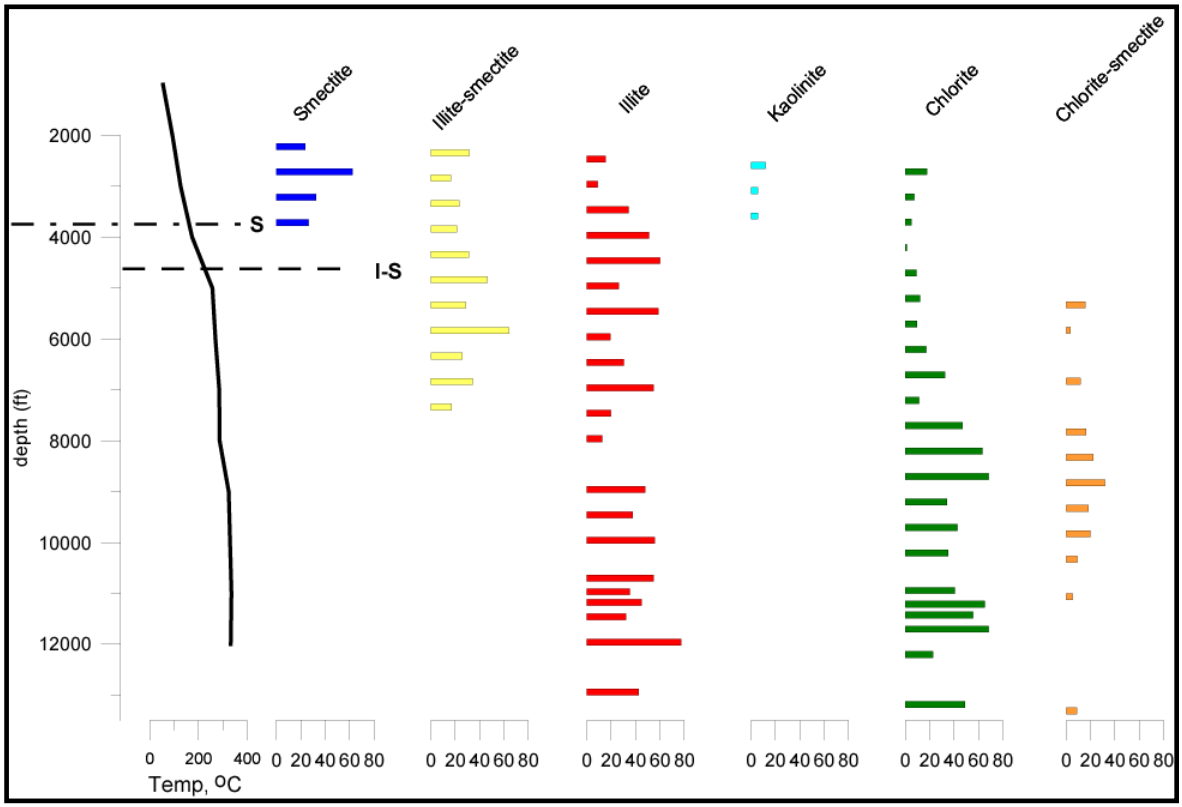

Fig. 13. Clay mineralogy as percent abundance of total clays versus depth for well 46A-19RD. The present day temperature profile is shown at the left for comparison. See text for further discussion.

The Target Zone: 10,000 ft to Depth

The interval from 10,000 ft (3048 m) to TD in the well is of special interest, as this is the target zone selected for stimulation by hydrofracturing. Although no lost circulation zones were encountered in this interval, there are indications that this zone was at least somewhat permeable in the past.

Several zones containing tectonic breccia were identified in the well from petrographic analysis of the cuttings at depths greater than 9400 ft (2865 m). Frequently, both the feldspars and quartz are strained in these intervals. Zones of intense brecciation correlate with zones of strong alteration and/or increased veining. In many instances, the zones of tectonic brecciation are cut by veins of later calcite ± quartz ± adularia ± chlorite (Fig. 14).

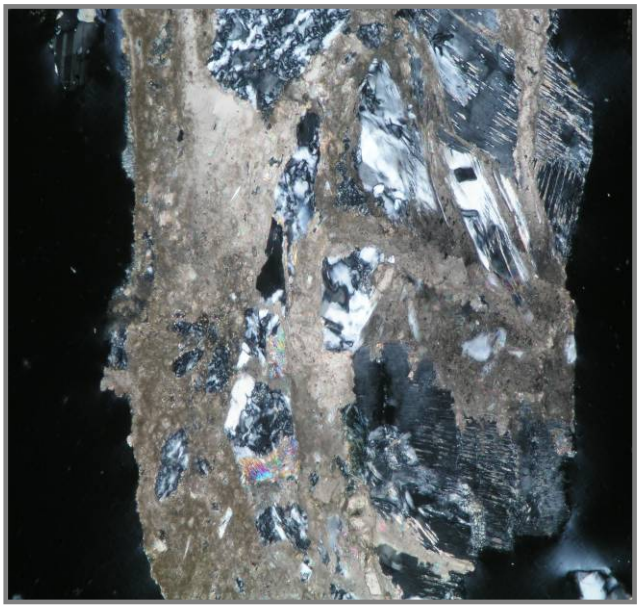

Fig. 14. Close-up of a calcite + chlorite vein in brecciated granodiorite.

In summary, the petrographic observations indicate that the most intensely brecciated and altered rocks in the zone targeted for stimulation (below 10,000 ft (3048 m)) occur between 11,200 and 11,350 ft (3414 and 3459 m). This zone is interpreted as a shear zone that initially juxtaposed quartz diorite against granodiorite. Strong pervasive alteration and veining within the brecciated quartz diorite and granodiorite suggest this shear zone was permeable in the past. This zone of weakness was subsequently exploited by a granophyre dike whose top occurs at 11,350 ft (3459 m). The dike is essentially unaltered. We anticipate, based on the cuttings samples that failure during stimulation will most likely occur along this shear zone.

The Salton Sea Geothermal System

The Salton Sea geothermal system is developed in Quaternary deltaic sandstones and shales of the Salton Trough, the northern landward extension of the Gulf of California (Fig. 15; Hulen and Pulka, 2001). Quaternary volcanoes are exposed at Obsidian Butte, Rock Hill, Red Island and Mullet Island and several of the wells have encountered older rhyolite (Hulen and Pulka, 2001). Injection well Elmore IW3 RD-1 was drilled in 1988 and used for injection until 1997. Fluids injected into Elmore IW3 RD-1 were

hypersaline (TDS exceeds 220,000 mg/kg) and metal-rich, but low in silica, which was removed prior to injection. The well was deepened in 1997 from 2308 to 2405 m depth due to declining performance and renamed Elmore IW3 RD-2.

Occurrence of Scale Deposits Within the Reservoir Rocks

A variety of scale deposits have been recognized in the cuttings from Elmore IW3 RD-2 based on their mineralogy and textures. Concentrations of scale occur primarily at the top of the redrill at a depth of approximately 2308 m and sporadically at greater depths (Fig. 16). Petrologic, SEM, and semiquantitative energy dispersive (EDX) analyses were used to determine the mineralogy and texture of the scale deposits found in the cuttings. Fluid inclusions were studied in associated euhedral calcite crystals to determine their petrogenesis.

Photomicrographs of scale deposits show distinct mineral banding that range from tens to hundreds of micrometers in thickness (Fig. 17; McLin et al., 2006c). SEM and EDX analyses demonstrate that the scale deposits consist of layers of barite and fluorite associated with minor anhydrite, amorphous silica and copper arsenic sulfides. Some bands of barite show strong Ti peaks in the EDX spectra, whereas amorphous silica bands show strong Fe peaks in the spectra. No differences in the chemistries of adjacent barite bands, was observed, suggesting that factors other than fluid chemistry control barite deposition. The anhydrite coats the barite, whereas the amorphous silica was found deposited on the copper arsenic sulfide scale.

Secondary fluid inclusions were studied in euhedral calcite crystals from a depth of 2308 m. Only two-phase liquid-rich inclusions were observed. The homogenization temperatures of thirty inclusions ranged from 337^{o} to 357^{o}C. These temperatures represent the minimum trapping temperatures. Ice-melting temperatures indicate salinities between 23 and 25 weight percent NaCl-$CaCl_2$ equivalent. These homogenization temperatures indicate that the calcite crystals were not formed as scale deposits, as these temperatures are much higher than the 110^{o}C and 258^{o}C temperatures of the injected fluid and the reservoir respectively.

The composition of the reservoir fluid was estimated from the composition of the production fluids from the Unit 6 Obsidian Butte well (Table 7). The fluid has an ionic strength of 2.2 M. Fe and Mg values were estimated from data tabulated by Hulen et al. (2004). Initial fluid compositions were calculated by equilibrating the reservoir fluid composition with each fluid regime at 258^{o}C, the initial reservoir temperature. The

Table 7. Composition of Unit 6 Obsidian Butte well.

Chemical Component	Mol/kg
SiO_2	.9962E-2
Na^+	.1957
K^+	.3325
Ca^{2+}	.6137E-1
Mg^{2+}	.1781E-5
Cl^-	3.944
F^-	.1053E-2
HCO_3^-	.1506E-2
SO_4^-	.1040E-2
Fe^{+2}	.2586E-6
Mg^{+2}	.1781E-5
Ba^{+2}	.1310E-2
pH	4.5

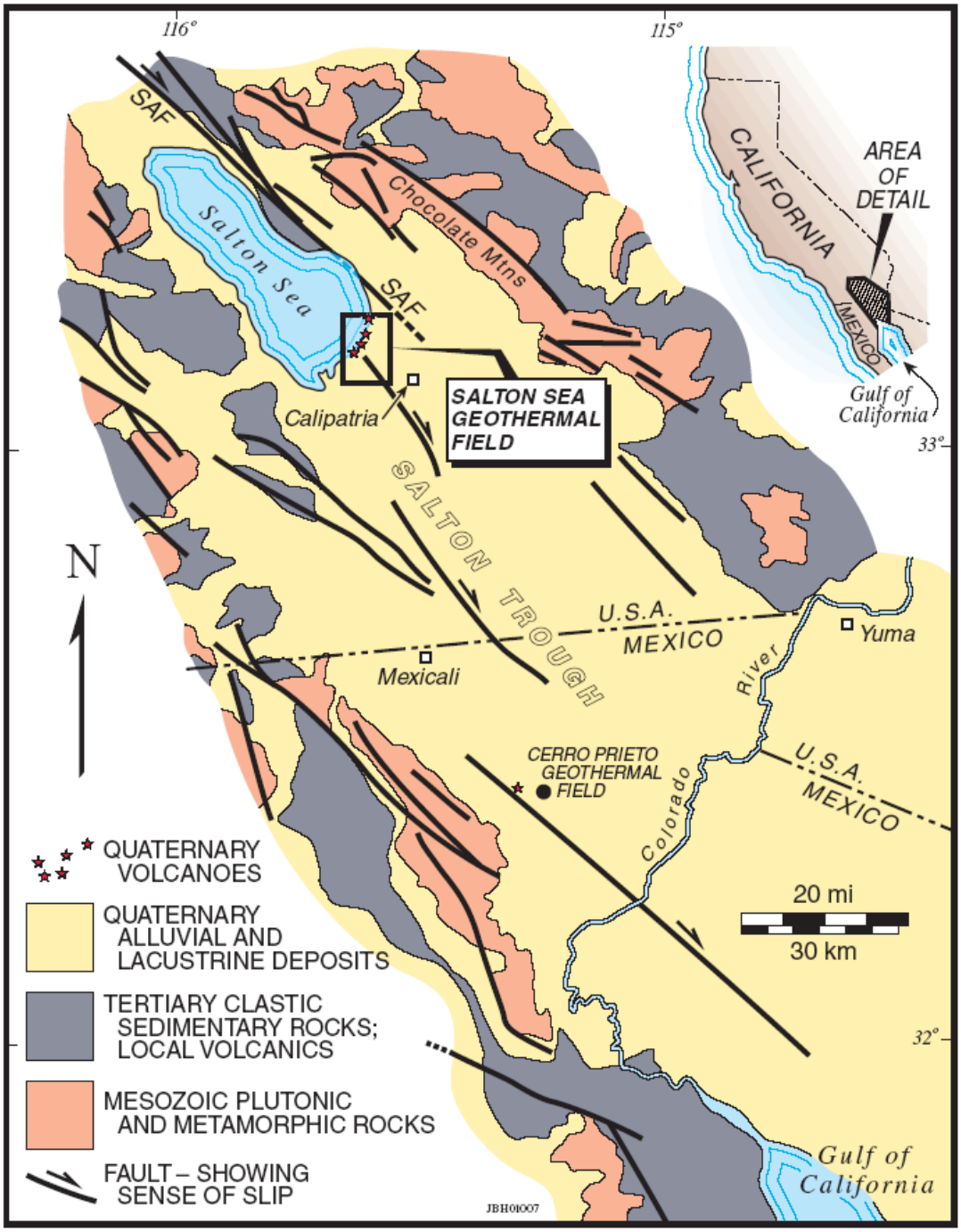

Fig. 15. Generalized geologic map of the Salton trough from Hulen et al., 2001.

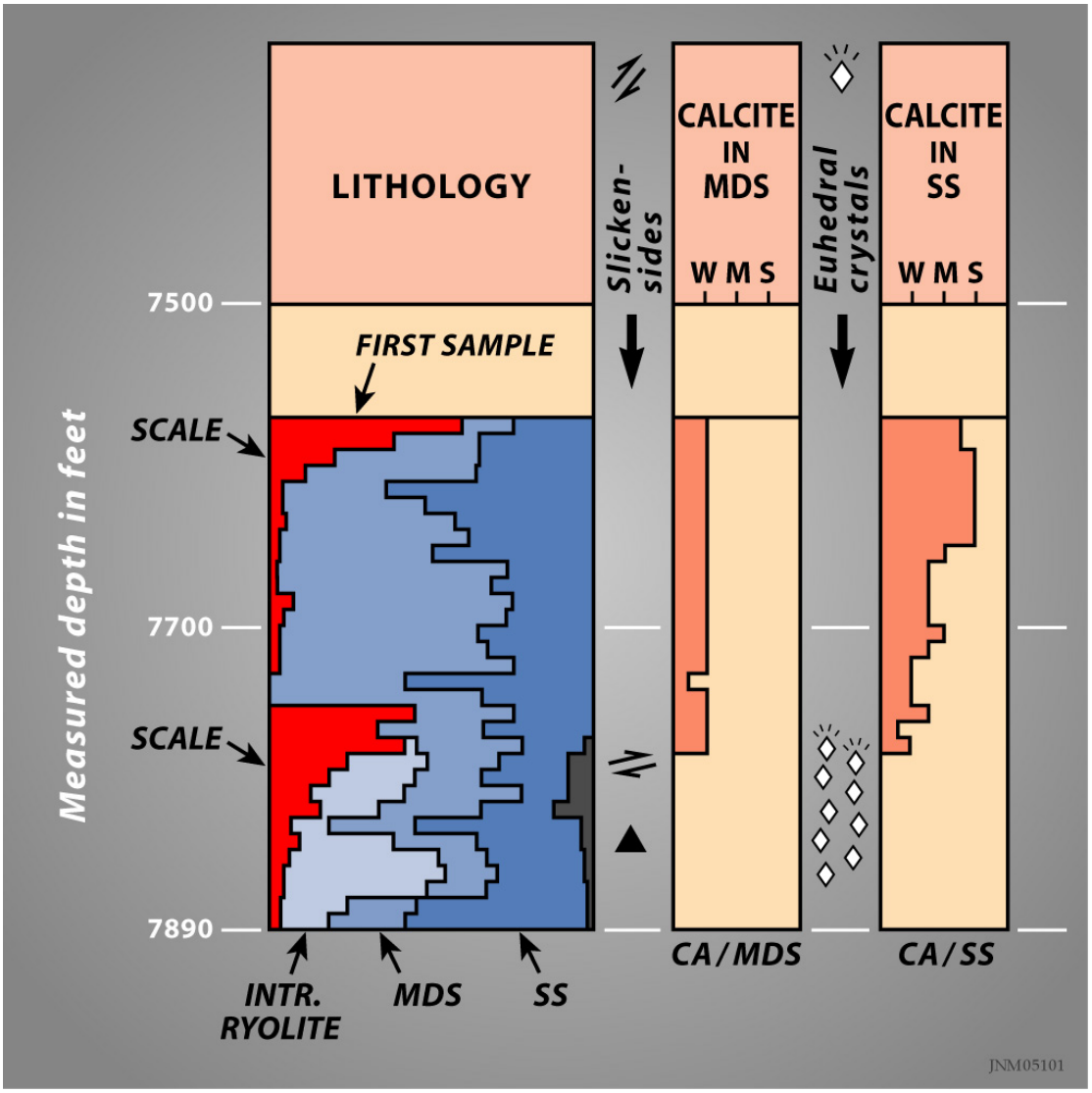

Fig. 16. Lithology of cuttings from Elmore IW3 RD-2 and calcite concentration, as well as the location of euhedral crystals and slickensides.

injectate composition was not allowed to change over time.

Geochemical Modeling of Fluid Rock Interactions

Geochemical simulations were carried out using the non-isothermal reactive geochemical transport code TOUGHREACT. An extended Debye-Huckel equation (after Helgeson et al., 1981) was used in this study for calculating the activity of aqueous species. Our conceptual model considers a one dimensional flow tube beginning at the injection well and extending outward for 500 m. The simulations were run for a total of 7 years. Changes in fluid pH, fracture porosity, fracture permeability, fluid temperature, and mineral abundances were monitored. Mineral abundance changes are reported in terms of changes in volume fraction of quartz, potassium feldspar, chlorite, illite, sodium

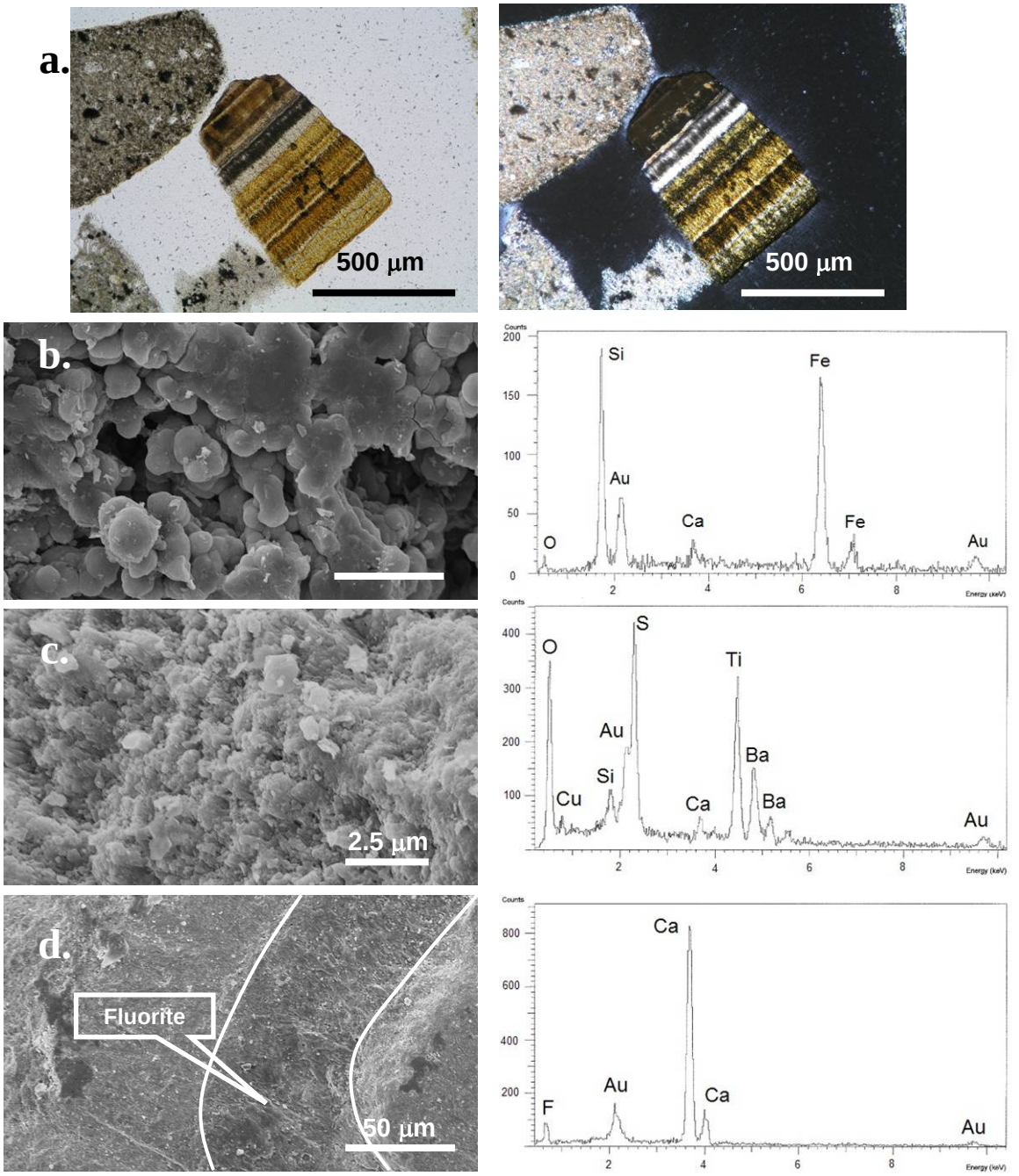

Fig. 17. (a) Photomicrographs of scale deposits from Elmore IW3 RD sampled from 2308-2405 m depth. Images taken under plane polarized light (left) and under crossed nicols (right). (b), (c), (d) SEM and corresponding EDX spectra for (b) amorphous silica (c) barite and (d) fluorite from scale deposits.

smectite, calcium smectite, calcite, dolomite, anorthite, biotite, amorphous silica, anhydrite, barite and fluorite. Calcite, barite, fluorite, anhydrite, quartz and amorphous silica displayed the most significant changes. Changes in porosity were calculated as a function of mineral dissolution and precipitation. Porosity increases when mineral dissolution is dominant, whereas porosity decreases when precipitation dominates. Changes in permeability are calculated from changes in porosity as described above.

Several different geochemical scenarios were simulated. In the initial model, the composition of the injected fluid was the same as the production fluid. The model results indicate that the deposition of amorphous silica, calcite, and quartz would be responsible for the porosity declines in Elmore IW3 RD. Barite and fluorite are minor precipitates, whereas anhydrite dissolves. As in the alternative models, fluorite precipitation continues after deposition of barite ceases. This model does not fit the observed mineralogy of the scales.

In the second simulation, the concentration of SiO_2 in the injection fluid was reduced to 10^{-22}, reflecting precipitation of SiO_2 prior to injection. In this case, amorphous SiO_2 does not precipitate, but a minor amount of quartz dissolves and then reprecipitates. Thus, the amorphous SiO_2 must be carried in the injection fluid and could not be derived through dissolution of the reservoir rock. In contrast to the initial model, Figure 18 shows that significant barite and calcite and minor fluorite precipitate. However, barite precipitation reaches a maximum at a later time, compared to the initial model.

Figure 19 shows the results of reducing both silica and HCO_3^- concentrations in the injection fluid. Reducing HCO_3^- in the injection fluid to trace amounts eliminates calcite precipitation, consistent with the observed scale mineralogy. In this model, barite and fluorite are the dominant phases precipitated, with fluorite deposition continuing after barite deposition ceases. This model results in the greatest amount of barite precipitation, which reaches a maximum value at still greater times than in the second model. Thus, this model best explains the observed mineral banding of the scale deposits.

The modeled results most closely simulate the observed mineral deposits based on observations of the cuttings samples when SiO_2 and HCO_3^- are reduced to trace amounts in the injection fluid. Because minor amounts of amorphous SiO_2 are found in the scale deposits, the model indicates that amorphous silica must at times be present in the injection fluid.

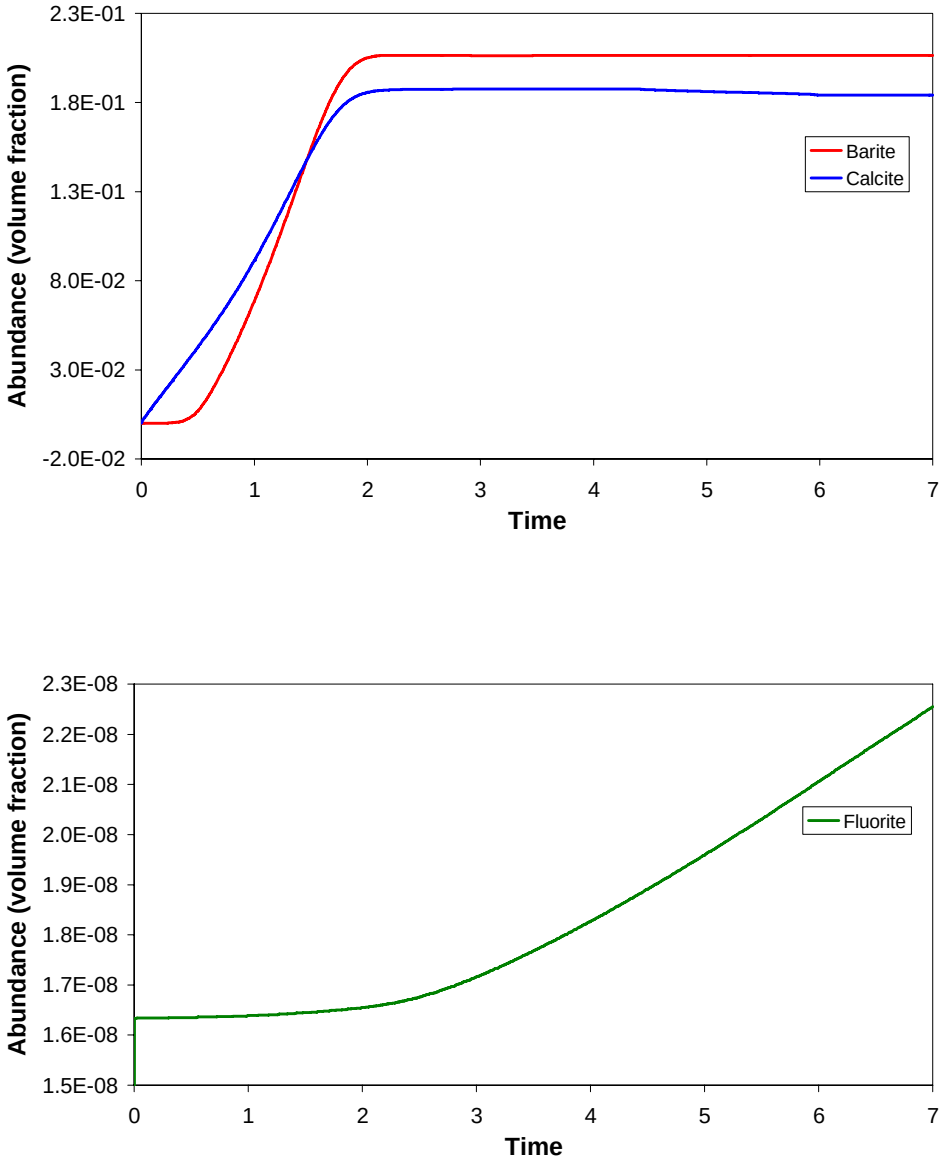

Figure 18. Graphs showing barite, calcite, and fluorite precipitation over time for the case in which SiO_2 is removed from the injection fluid.

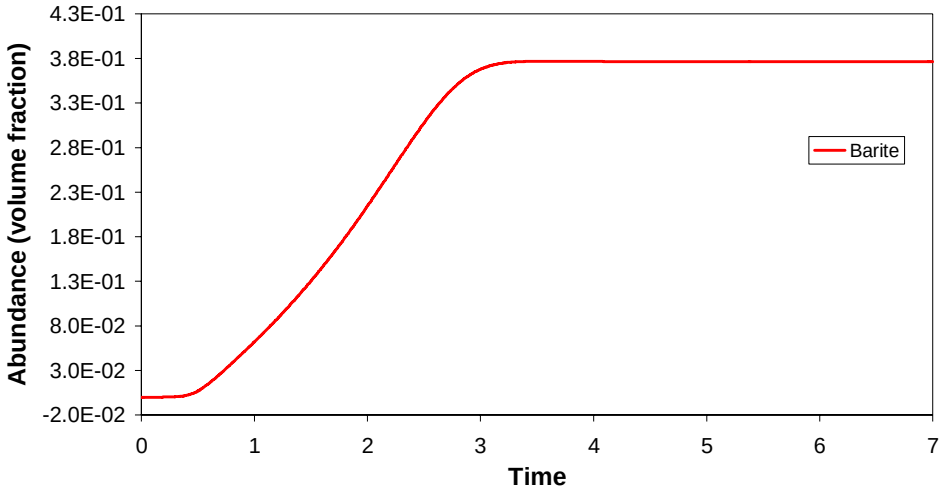

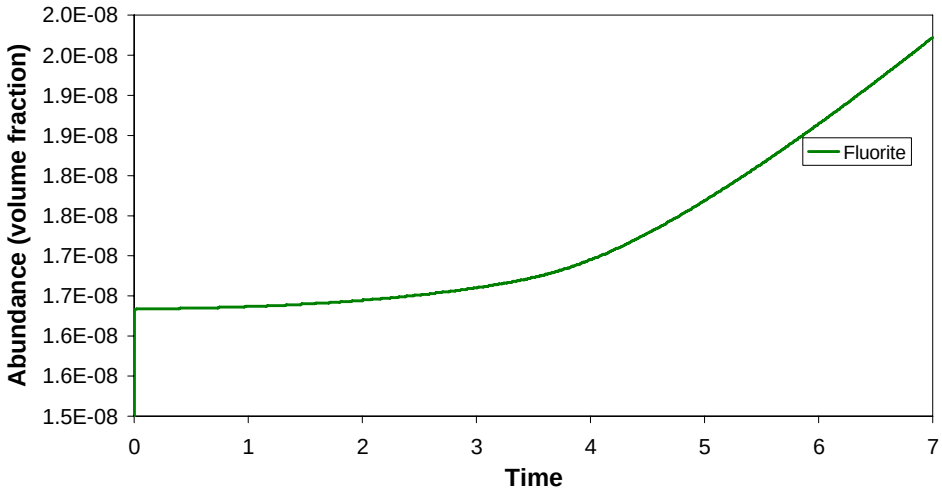

Fig. 19. Graphs showing barite and fluorite precipitation over time for the model with silica and bicarbonate removed from the injection fluid.

Reports Resulting from this Project

Dilley, L, Norman, D.I., Moore, J. and McCulloch, J., (2006). "Fluid stratigraphy and permeable zones of the Coso geothermal reservoir". Geothermal Resources Council Transactions, v. 30, p. 127-131.

Kovac, K.M., Moore J.N., Rose P.E. and McCulloch J. (2006) "Geology of injection well 46A-19RD in the Coso Enhanced Geothermal Systems experiment." Geothermal Resources Council Transactions, v. 30, p. 139-143.

McLin, K.S., Moore, J.N., Hulen, J., Bowman, J.R., Berard, B. (2006a) "Mineral characterization of scale deposits in injection wells; Coso and Salton Sea geothermal fields, CA." Proceedings, 31st Workshop on Geothermal Reservoir Engineering.

McLin, K.S., Kovac, K.M., Moore, J.N., Adams, M.C., Xu, T. (2006b) "Modeling the Geochemical Effects of Injection at Coso Geothermal Field, CA; Comparison with Field Observations" Proceedings, 31st Workshop on Geothermal Reservoir Engineering.

McLin, K.S., Kovac, K.M., Moore, J.N., Kaspereit, D., Berard, B., Xu, T., McLin, R.H., Hulen, J.B. (2006c) "Modeling the Geochemical Effects of injection at Salton Sea geothermal field, California: comparison with field observations." Geothermal Resources Council Transactions, v. 30, 507-511.

Norman, D.I, Dilley, L, McLin, K.m and Moore, J.N., (2006), "Applying fluid inclusion stratigraphy analyses to geothermal systems." 16th V. M. Goldschmidt Conference, Melbourne, Australia, 27 August-01 September 2006.

Park, J., Norman, D., McLin, K. and Moore, J. (2006) "Modeling amorphous silica precipitation: a strategy to reduce silica precipitation near Coso injection wells." Proceedings, 29th Workshop on Geothermal Reservoir Engineering, Stanford University.

References

Adams, M.C., Moore, J.N., Bjornstad, S., and Norman, D.I. (2000) "Geologic history of the Coso geothermal system." Geothermal Resources Council Transactions, v. 24, p. 205-209.

Bachler, D. (2003) "Coupled thermal-hydraulic-chemical modeling at the Soultz-sous-Forets HDR reservoir" (France). PhD dissertation, Swiss Federal Institute of Technology, Zurich, Switzerland.

Dilley, L, Norman, D.I., Moore, J. and McCulloch, J., (2006). "Fluid stratigraphy and permeable zones of the Coso geothermal reservoir". Geothermal Resources Council Transactions, v. 30, p. 127-131.

Durst, D. (2002) "Geochemical modeling of the Soultz-sous-Forets hot dry rock test site: Coupled fluid-rock interaction to heat and fluid transport." PhD dissertation, Universite de Neuchatel, France.

Fournier, R.O. (1985) "The behavior of silica in hydrothermal solutions" in: B.R. Berger and P.M. Bethke, eds., Geology and Geochemistry of Epithermal Systems, Reviews in Economic Geology, v. 2, Society of Economic Geologists, p. 45-61.

Gunnarsson, I. and Arnorsson, S. (2000) "Amorphous silica solubility and the thermodynamic properties of $H_4SiO_4^o$ in the range of 0^o to 350^oC at P_{sat}." Geochimica and Cosmochimica Acta, v. 64, 2295-2307.

Helgeson, H.C., Kirkham, D.H., Flowers, D.C. (1981) "Theoretical prediction of the thermodynamic behavior of aqueous electrolytes at high pressures and temperatures: IV. Calculation of activity coefficients osmotic coefficients, and apparent molal and standard and relative partial molal properties to 600^{o}C and 5 kb." American Journal of Science, v. 281, 1249-1516.

Hulen, J.B. and Pluka, F.S. (2001) "Newly-discovered, ancient extrusive rhyolite in the Salton Sea geothermal field, Imperial Valley, Californial." Proceedings, 26th Workshop on Geothermal Reservoir Engineering.

Hulen, J.B., Norton, D.L., Moore, J.N., Kaspereit, D. (2004) "Epithermal vein-hosted and stratabound Pb-Zn mineralization in an active hydrothermal system: the southern Salton Sea geothermal field, California." Geothermal Resources Council Transactions, 28, 415-424.

Iler, R.K. (1979) The Chemistry of Silica-Solubility, Polymerization, Colloid, and Surface Properties, and Biochemistry. John Wiley & Sons, Inc., New York.

Kovac, K.M., Moore, J.N., and Lutz, S.J. (2005) "Geologic framework of the East Flank, Coso geothermal field: Implications for EGS Development." Proceedings, 30th Workshop on Geothermal Reservoir Engineering.

Kovac K.M., Moore J.N., Rose P.E. and McCulloch J. (2006) "Geology of injection well 46A-19RD in the Coso Enhanced Geothermal Systems experiment." Geothermal Resources Council Transactions, v. 30, p. 139-143.

Lutz, S.J., and Moore, J.N. (1997) "Petrographic and X-ray diffraction study of 130 cuttings samples from six wells in the Coso geothermal area, California," unpublished CalEnergy Corporation Report.

Lynne, B.Y., Campbell, K.A. (2004) "Morphologic and mineralogic transitions from opal-A to opal-CT in low-temperature siliceous sinter diagenesis, Taupo Volcanic zone, New Zealand." Journal of Sedimentary Research, v. 74, n. 4, p. 561-579.

McLin, K.S., Moore, J.N., Hulen, J., Bowman, J.R., Berard, B. (2006a) "Mineral characterization of scale deposits in injection wells; Coso and Salton Sea geothermal fields, CA." Proceedings, 31st Workshop on Geothermal Reservoir Engineering.

McLin, K.S., Kovac, K.M., Moore, J.N., Adams, M.C., Xu, T. (2006b) "Modeling the Geochemical Effects of Injection at Coso Geothermal Field, CA; Comparison with Field Observations" Proceedings, 31st Workshop on Geothermal Reservoir Engineering.

McLin, K.S., Kovac, K.M., Moore, J.N., Kaspereit, D., Berard, B., Xu, T., McLin, R.H., Hulen, J.B. (2006c) "Modeling the Geochemical Effects of injection at Salton Sea geothermal field, California: comparison with field observations." Geothermal Resources Council Transactions, v. 30,507-511.

Norman, D.I, Dilley, L, McLin, K.m and Moore, J.N., (2006), "Applying fluid inclusion stratigraphy analyses to geothermal systems." 16th V. M. Goldschmidt Conference, Melbourne, Australia, 27 August-01 September 2006.

Park, J., Norman, D., McLin, K. and Moore, J. (2006) "Modeling amorphous silica precipitation: a strategy to reduce silica precipitation near Coso injection wells." Proceedings, 29th Workshop on Geothermal Reservoir Engineering, Stanford University.

Pruess, K., Oldenburg, C., Moridis, G., 1999. TOUGH2 user's guide, Version 2.0. Lawrence Berkeley Laboratory Report LBL-43134, Berkeley, California.

Palandri, J.L. and Kharaka, Y.K. (2004). A compilation of rate parameters of water-mineral interaction kinetics for application to geochemical modeling. U.S. Geological Survey Open File Report 2004-1068.

Rodgers, K.A., Browne, P.R.L., Buddle, T.F., Cook, K.L., Greatrex, R.A., Hampton, W.A., Herdianita, N.R., Holland, G.R., Lynne, B.Y., Martin, R., Newton, Z., Pastars, D., Sannazarro, K.L., Teece, C.I.A. (2004) "Silica Phases in sinters and residues from geothermal fields of New Zealand." Earth Science Reviews, v. 66, p. 1-61.

Vinsome, P. K. W., and J. Westerveld, 1980. A simple method for predicting cap and base rock heat losses in thermal reservoir simulators. Journal of Canadian Petroleum Technology, v. 19 (3), 87–90.

Xu, T. and Pruess, K. (2001) "Modeling multiphase non-isothermal fluid flow and reactive geochemical transport in variably saturated fractured rocks: 1. Methodology." American Journal of Science, v. 301, 16-33.

Xu, T. and Pruess, K. (2004) "Numerical simulation of injectivity effects of mineral scaling and clay swelling in a fractured geothermal reservoir." Geothermal Resources Council Transcations, v. 28, 269-276.

Xu, T., Sonnenthal, E., Spycher, N., and Pruess, K. (2004) "TOUGHREACT user's guide: A simulation program for non-isothermal multiphase reactive geochemical transport in variably saturated geologic media." Lawrence Berkeley National Laboratory publication LBNL-55460.